



Design and implementation of a cable-driven parallel robot for additive manufacturing applications

Damien Gueners, Hélène Chanal, Belhassen-Chedli Bouzgarrou

► To cite this version:

Damien Gueners, Hélène Chanal, Belhassen-Chedli Bouzgarrou. Design and implementation of a cable-driven parallel robot for additive manufacturing applications. *Mechatronics*, 2022, 86, pp.102874. 10.1016/j.mechatronics.2022.102874 . hal-03752992

HAL Id: hal-03752992

<https://uca.hal.science/hal-03752992>

Submitted on 17 Aug 2022

HAL is a multi-disciplinary open access archive for the deposit and dissemination of scientific research documents, whether they are published or not. The documents may come from teaching and research institutions in France or abroad, or from public or private research centers.

L'archive ouverte pluridisciplinaire **HAL**, est destinée au dépôt et à la diffusion de documents scientifiques de niveau recherche, publiés ou non, émanant des établissements d'enseignement et de recherche français ou étrangers, des laboratoires publics ou privés.



Distributed under a Creative Commons Attribution - NonCommercial - NoDerivatives 4.0 International License

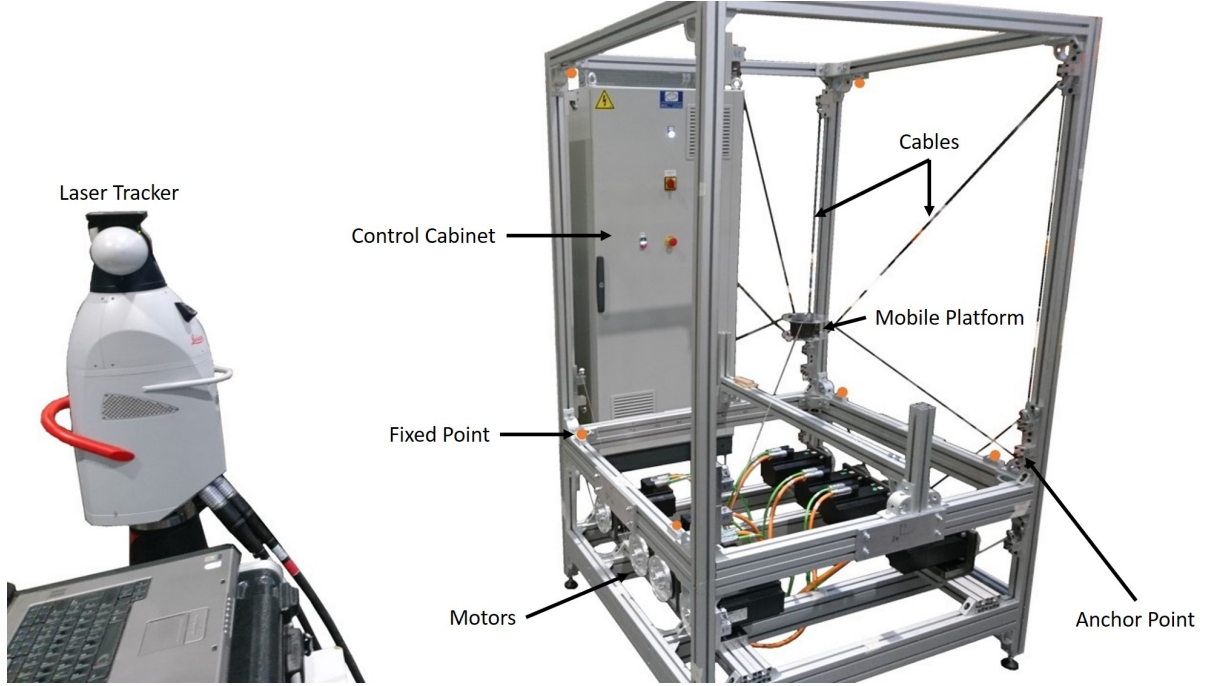


Figure 1: The experimental setup consisting of the prototype with the laser tracker. Six fixed points on the robot frame represented by the orange dots are used for calibration.

experimentally that increasing the cable preload increases the robot stiffness. In this paper, the robot performances are evaluated for two 2 different MPF designs, which corroborates previous researches on the robot anchor point position optimization. The influence of the cables preload is analyzed on the robot dynamic performance.

Section 2 introduces the mechanical design and the control cabinet of the CDPR prototype. This section presents a state of the art of different technological solutions used in CDPRs. Then, the geometric model, which determines the cable lengths as a function of the platform position for the trajectory planning is detailed in Section 3. The robot parameters are determined by a calibration process using a laser tracker and the motor output measurements (torque and angle). In Section 4, the geometric and dynamic performance of the CDPR equipped with two different platforms are analyzed and discussed for a horizontal circular trajectory with 0.1 m radius and 6.28 s duration.

2. CDPR prototype design

The robot design is based on a state of the art analysis of the different elements that compose a CDPR. This section presents the hardware used on the robot. Controlling the robot mechanical behavior can significantly improve its performance. The CDPR mechanical design consists in selecting the cables, the winding cable system, the fixed base and the MPF. The robot frame is an assembly of 45 mm × 45 mm and 45 mm × 90 mm aluminum profiles that allow us to easily mount the different parts.

2.1. The cables

The cables are the elements that link the CDPR mobile platform to a fixed base frame. They significantly influence the robot performance. Depending on the cable material, the observed mechanical phenomena are different. The cable tensile stiffness [12, 17, 18] is the most considered characteristic in the literature, as the robot stiffness is a major behavior which should be controlled to guarantee an accurate toolpath following. In addition to the cable tensile stiffness, other mechanical properties related to the cables can influence the CDPR performance such as hysteresis [19, 20, 21], damping [20] and creep [22]. The cable lifetime also affects the CDPR maintenance strategy [23, 24]. The cable lifetime is mainly reduced by the friction on the anchor points. In the case of large space application with heavy cables, these ones can sag, making their modeling more complex [2].

The cables of the robot was chosen after experimental characterizations of three different materials of rope (steel, aramid, ultra-high-molecular-weight polyethylene) that can be seen in a previous article by the authors [16]. In comparison with polymer ropes, steel cables do not have creep and are more appropriate for 3D-printing applications. The cable used for the prototype is in braided stainless steel with 7 strands and a diameter of 0.54 mm from Carl Stahl. The cable elastic modulus is 69.49 GPa determined experimentally on a viscoanalyzer. From the constructor datasheet, the maximum charge before rupture is 235 N. A thin cable is sufficient to support a 3D printer platform (with a mass of less than 2 kg). This allows also neglecting cable sagging to simplify the geometric model. To actuate the cable a winch is necessary.

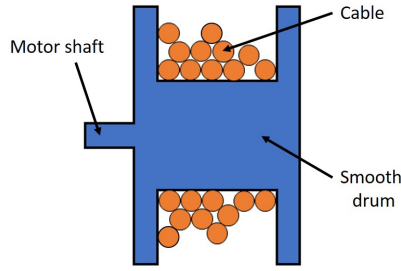


Figure 2: Winch with uncontrolled cable winding (cut-away view)

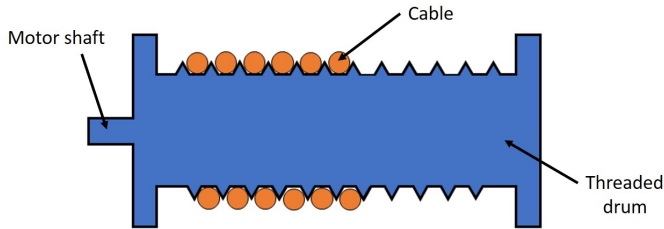


Figure 3: Threaded winch (cut-away view)

2.2. The winch

The winch is the most complex mechanical part of a CDPR. The majority of CDPRs use electric motors to control the cable lengths. An inaccurate winch generates a high geometric error, so its design will directly influence the robot performance. The most common industrial solution is a winch where the cable is wound around (Figure 2). This solution is used in particular on Marionet [25], Calowi [26] or [27] robots. The cable winding is free, which makes it impossible to control the winding on the winch. The majority of CDPRs use encoders to measure the angle of the winch. This solution is not accurate as the cable exit point is hazardous. The use of a complementary measuring system is necessary [28].

To prevent the cable winding on the winch from being random, it is useful to add a thread on the winch to constrain the lateral winding of the cable (Figure 3). This solution improves cable winding precision and is now the most widely used solution on CDPRs [12, 29, 4, 30, 3, 31, 32, 33, 34, 35]. But the downside of this solution is that it doesn't maintain a fixed cable exit point. It is necessary to integrate the position of the cable on the winch on the geometric model of the robot to improve accuracy. It is also possible to move the intermediate pulley as far away as possible from the winch so that the variation in cable length caused by the displacement of the exit point is negligible.

A third solution is to move the winch in translation in addition to its rotation. This solution uses a drive screw combined with translational guidance to achieve this movement (Figure 4). If the reduction ratio between the pitch of the drive screw and the diameter of the winch is correctly chosen, the cable exit point remains fixed. This solution is present in the robots studied in the following articles [36, 37, 38, 39, 40, 41]. However, the dynamic performance of this solution is not as good as the

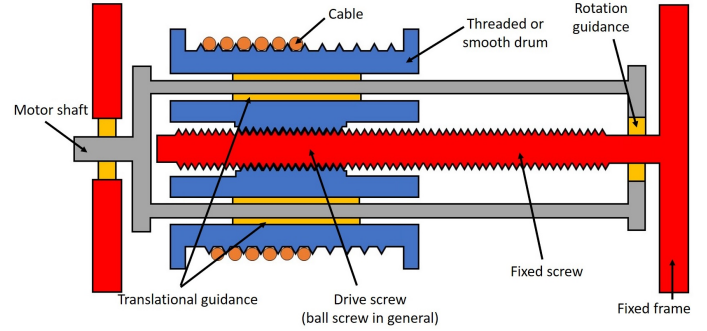


Figure 4: Rotating and translating winch by means of a screw link (cut-away view)

previous two. In fact, the translational and rotational inertia of the winch degrades dynamic performance. In addition, the drive screw and translational guidance add friction. This solution is also more bulky than the previous two.

Other solutions appear to assist in guiding the cable on the winch or to have a fixed point at the assembly outlet. It is possible to use a rotating threaded winch with the help of a fixed cable exit point (Figure 5). This exit point can be just a simple hole as in [42, 43, 29]. To reduce the friction of the cable, the hole can be replaced by a pulley with 2 degrees of freedom in rotation [44]. A more complex solution present on the Charlotte robot [8, 45] is to combine a pulley which moves in translation to help wind the cable synchronously with the rotation of the winch and add a fixed exit point with a hole (Figure 6). The IPAnema 3 robot uses a similar winding by replacing the single hole by a pulley with 2 degrees of freedom [3]. A Technalia patent [46] relies on adding 2 sensors to the output pulley to measure the cable exit angle. The Skycam [47] winch does not have a thread, but uses cable winding guidance with pulleys, translational guides and a drive screw. These solutions are more complex to implement.

Other solutions for driving the cable exist, such as the NIMS3D which uses a fishing rod winch to wind the cable [48]. For short cable length, it may be possible to replace the winch with a linear actuator as in [49, 3, 50]. The linear actuator can be combined with a hoist system to increase the cable length [49]. But on the other hand, the force that the motor can generate in the cable is reduced. For low amplitude movements as on the WARP [51] or [52], it is possible to replace the winch with a rigid arm. This system is similar to string puppets. In [53], a 5 bar parallel robot is proposed instead of a winch.

The winches can handle the winding of several cables as in [7, 29, 54, 55, 13, 50]. This solution can make it possible to constrain certain degrees of freedom of the platform, increase the workspace, and also the rigidity of the robot. It is also possible to have an additional balancing cable on the winch to keep a preload on the cable when the motor is powered off as shown on the INCA robot [56].

The winding system is one of the key points. In the state of the art, we can see a complex winding system on the CDPRs. The technical implementation of our robot favours simple, but mechanically precise solutions. The radial winding of the cable

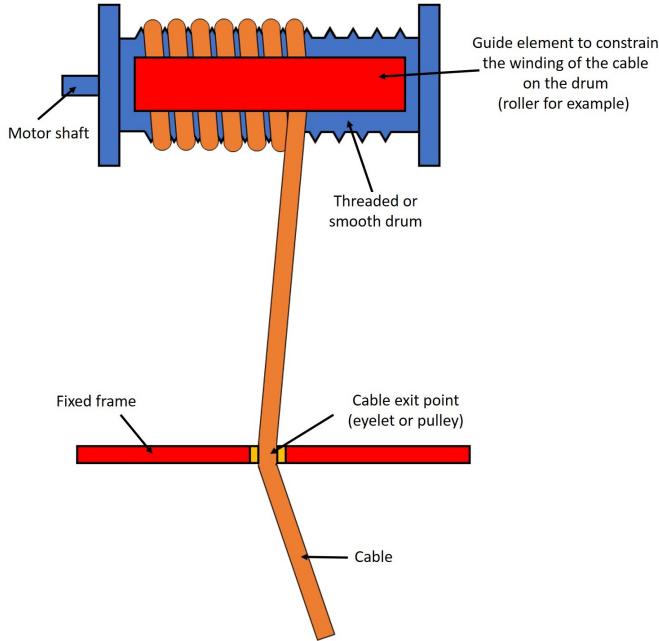


Figure 5: Winch with a fixed exit point.

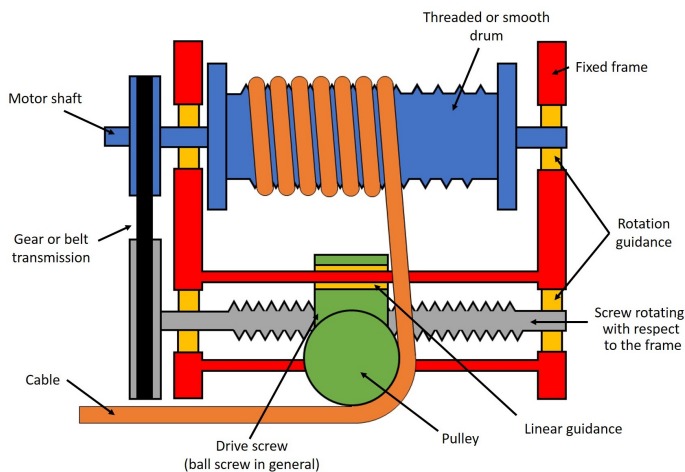


Figure 6: Winch with rope guidance by means of a pulley and a screw connection.

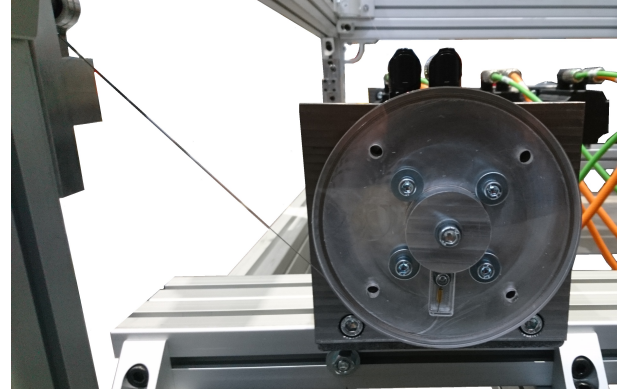


Figure 7: Radial cable winding solution.

on a disk was chosen because the study of this solution has advantages over the solutions already present on the CDPRs. This solution is possible for small lengths of cable to be wound. In our case this length is less than 2 meters. The geometrical modeling of this winch will also be discussed in Section 3. This solution puts forward advantages or disadvantages not previously discussed in the literature. It is important to see if the estimation of the force in the cables directly from the motor torque is possible or if the addition of an extra force sensor is necessary.

The winding solution is shown in Figure 7. The disk radius is 60 mm and the cable slot is 0.6 mm wide. This solution allows us to reduce the geometric error caused by the cable roll on the disk. The radius was chosen according to the motor characteristics and the desired performance in terms of precision and force. The winding system is in two parts. The first part was manufactured in aluminum. The second was laser cut from plexiglas. The transparent side allows us to visualize the cable winding. The cable access on the disk can be seen in Figure 7. The disk is directly mounted on the motor shaft to limit the guidance friction. Undesired physical effects are mainly caused by disk inertia and static friction. The torque transfer between the motor and the disk is realized with a shaft key. The disk position on the robot frame is measured with a Leica laser tracker. Four holes on the side are used to fix the laser tracker ball. With these holes, the disk position can be determined. A steel mounting bracket machined in two parts is used to fix the motor to the frame. Intermediate pulleys are used to guide the cables between the disk and the mobile platform.

2.3. Anchor points

Anchor points are used to determine the CDPR geometric model. These points are attached to the fixed frame, to the MPF or used to change the cable direction. They are also used to decrease cable friction. Intermediate anchor points can be single holes [27] or with ceramic guidance [12] to reduce the shear due to cable friction. But the most commonly used solution on parallel cable robots are deflection pulleys. These pulleys can have a V groove [26, 31, 50] commonly used in lifting applications which allow more freedom to the cable or pulleys machined with a groove adapted to the diameter of the cable [37, 40]. The pulleys can be fitted with plain bearings or ball bearings. On

CDPRs, these pulleys can have more than one degree of freedom. In the case of a pulley with 2 DOFs, it is common to have an axis of rotation of the pulley aligned with the direction of the cable [3, 37, 40, 34, 32], thus, one pulley anchor point can be considered constant on the fixed frame (Figures 8 c,d,f,g,h). The intermediate anchoring points can include additional guides (Figure 8 g,h for example) as in [57, 37, 30]. Eight possible design solutions for intermediate anchoring points are shown in Figure 8.

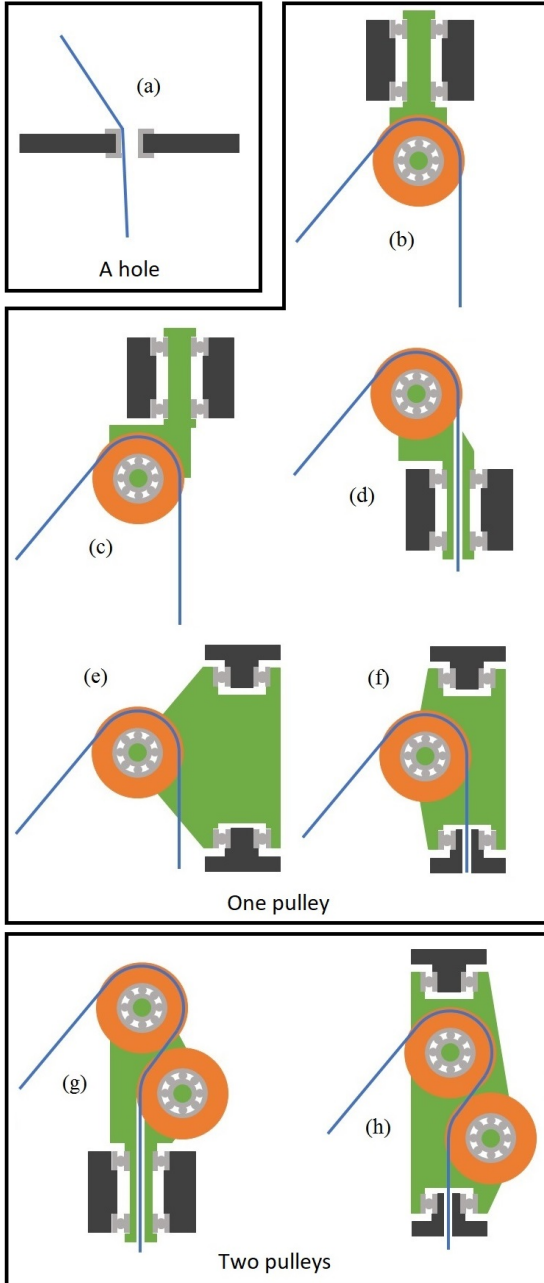


Figure 8: Some possible intermediate anchor point configurations.

In our case, we choose a cables' geometric routing system similar to that of the Mini IPanema [58] can be seen in Figure 13. This solution is easy to add to the geometric model and it

allows us to switch the cable direction with only low friction. The shaft and support of the pulley are in steel. The pulley in contact with the cable is in aluminum. The aluminum pulley has a semi-V slot (Figure 9) realizable with a standard lathe machine. The shafts are configurable mechanical parts of Misumi. The other parts to fix the anchor point on the robot frame are machined in aluminum. The vertical guidance is in a polymer slide bearing from Igus. The guidance for the pulley is a standard ball bearing. These pulleys allow us to guide the cable which move the platform.

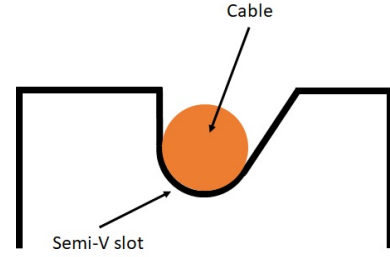


Figure 9: Semi-V split of the intermediate pulleys.

2.4. The Mobile Platform (MPF)

The MPF also has an influence on the CDPR geometric errors. Its design process should enable us to determine the anchor points. The method by which the cable is fixed on the MPF depends mainly on the diameter and type of the cable. For applications with smaller cable diameters, the attachment to the platform is via a knot or the cable is crimped through a hole [12, 29, 39, 40, 33, 50, 59] (Figure 10 a). The hole can also be conical as for the MiniIPanema [60] (Figure 10 b) to reduce shear stress. For larger scale applications, fittings are used [6, 25, 61, 62, 34] (Figure 10 c). However, the fittings do not guarantee the position of a fixed anchor point on the platform. Patents of Fraunhofer [63] and Tecniaia [46] use additional guidance elements to ensure that the anchor point is correctly estimated (Figure 10 d). In [38], a design using a pulley as an anchor point on the platform allows a simplified geometric model to be kept without considering the radius of the robot intermediate pulley (Figure 10 e). But this solution only works with a planar CDPR or by pre-defining the orientation of the robot platform. Some robots such as the Charlotte [8, 45] have their engines directly on the MPF. Figure 10 summarizes various fixing solutions on the MPF.

Two geometric MPFs viewable in figures 11 are studied. The first one has a shape close to a parallelepiped. The MPF anchor points are on upper and lower planes with a vertical plane symmetry. A particularity of this MPF is that the cables are crossed as in the IPanema robot family [58]. We call this MPF Init X and the second one Optim. For the second platform, the anchor point positions have been determined to maximize the MPF rigidity inside the printing space [15]. The collision between the cables and the part to be printed inside the wrench-feasibility workspace has been considered in [15]. The printing space is shown in Figure 12. As we have assumed that the orientation of the platform is constant, there is no possibility of

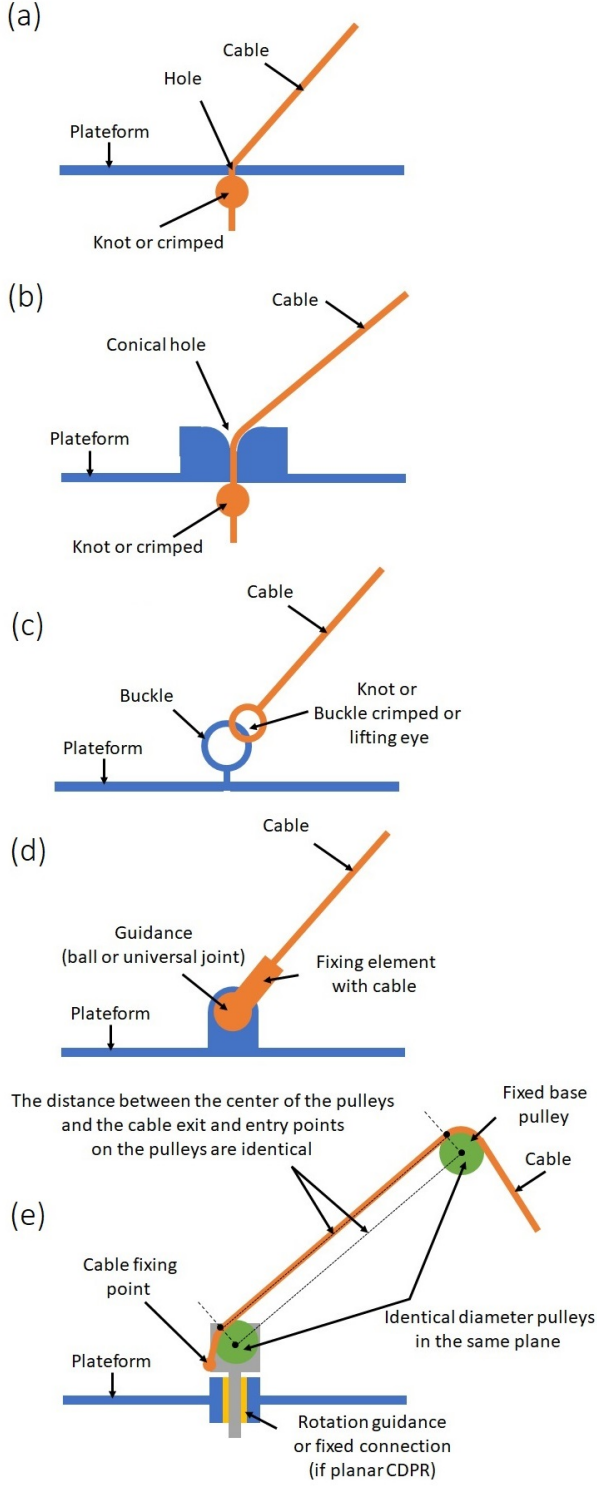


Figure 10: Suggested mounting configurations on the platform

collision between the cables. Moreover, the Optim design of the MPF helps to avoid collisions between the cables, as they are connected on the same plane. From the authors' previous work [16], the optim MPF has a better rigidity than the init X MPF on a prototype without motors. The platforms are in 5 mm plexiglass plate. A laser cutting machine enables a small hole

to be made so that the crimped cable may threaded through. A steel cylindrical mass of 2.4 kg is added on both platforms. The large holes on the platforms are for positioning the laser tracker ball and measuring the pose. The MPF anchor point positions are resumed in Table 1.

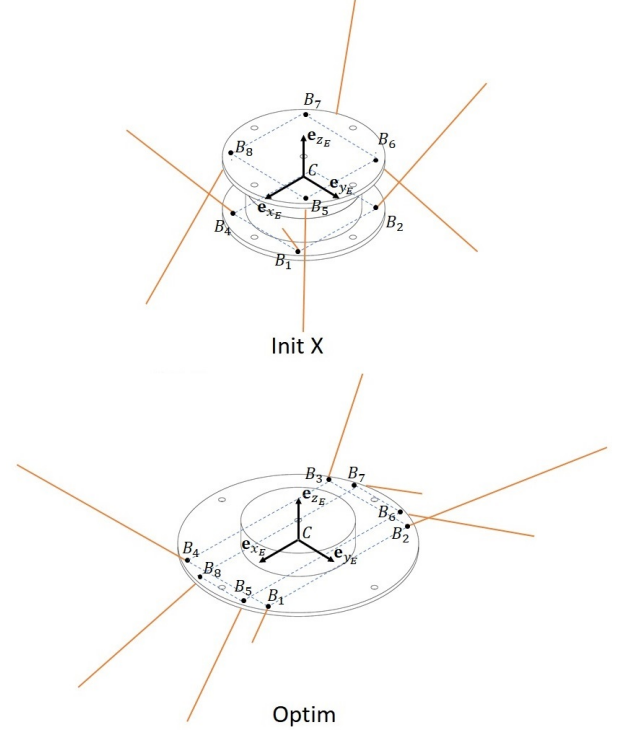


Figure 11: CAD view of Init X and Optim platforms.

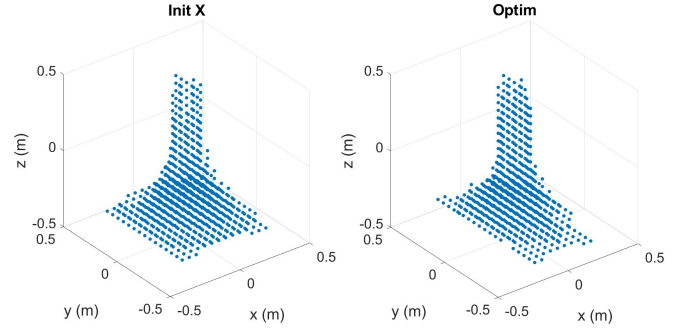


Figure 12: Printing space of Init X and Optim platforms.

This simple design makes it easier to identify the geometric parameters of the robot.

2.5. The motors

The motor should be chosen at the same time as the winch. It should be properly dimensioned so that reach the winding speed and the desired tensile force of the cable. The cheapest way to estimate tension in the cable is to use an estimation of motor torques from current measurements. But this solution shows its limits when friction is too high due to the transmission system. An additional force transducer is usually necessary. Force sensors can be added to the ends of the cables at the

	CB_1	CB_2	CB_3	CB_4
Init X	$\begin{bmatrix} 48.7 \\ -39.3 \\ -24.8 \end{bmatrix}$	$\begin{bmatrix} 47.3 \\ 41.1 \\ -25.1 \end{bmatrix}$	$\begin{bmatrix} -47.9 \\ 39.6 \\ -26.9 \end{bmatrix}$	$\begin{bmatrix} -46.5 \\ -40.8 \\ -26.6 \end{bmatrix}$
Optim	$\begin{bmatrix} 87.3 \\ -48.8 \\ 2.5 \end{bmatrix}$	$\begin{bmatrix} 87.3 \\ 48.8 \\ 2.5 \end{bmatrix}$	$\begin{bmatrix} -87.3 \\ 48.8 \\ 2.5 \end{bmatrix}$	$\begin{bmatrix} -87.3 \\ -48.8 \\ 2.5 \end{bmatrix}$
	CB_5	CB_6	CB_7	CB_8
Init X	$\begin{bmatrix} 43.7 \\ -44.2 \\ 25.9 \end{bmatrix}$	$\begin{bmatrix} 43.7 \\ 43.9 \\ 25.9 \end{bmatrix}$	$\begin{bmatrix} -44.5 \\ 43.9 \\ 25.9 \end{bmatrix}$	$\begin{bmatrix} -44.5 \\ -44.2 \\ 25.9 \end{bmatrix}$
Optim	$\begin{bmatrix} 96.2 \\ -27.3 \\ -2.5 \end{bmatrix}$	$\begin{bmatrix} 96.2 \\ 27.3 \\ -2.5 \end{bmatrix}$	$\begin{bmatrix} -96.2 \\ 27.3 \\ -2.5 \end{bmatrix}$	$\begin{bmatrix} -96.2 \\ -27.3 \\ -2.5 \end{bmatrix}$

Table 1: MPF anchor points positions (in mm) on the MPF frame.

anchor points of the platform [64, 60, 65, 66]. But this solution requires running electric cables to the platform or equipping the platform with on-board electronics. A force sensor can be added to an intermediate pulley as in [67, 12, 30, 40, 41, 44]. It is necessary for the direction of the cable with respect to the force transducer to be known. A cable routing system using pulleys may therefore be necessary [26]. In [68], a maximum error greater than 1 N is observed between the force of the sensor and the theoretical estimate. This difference is mainly due to the presence of vibrations (largely due to the low rigidity of the elements and the cable) and the friction of the pulleys. On the IPanema3 robot, the force is estimated using a force sensor integrated into the cable winding system on the winch [3]. The measurement of the force can also be estimated using the measurement of the force applied by the cable on the pulleys [31] or by replacing the shaft with a load pin as on the WARP [51] and HRPCable [69].

The robot motors used are eight SMHA 10045065192I6S44 servomotors from Parker. They were chosen to avoid the use of a gear reducer to decrease the frictions. In this application, the motor works mainly on these slow characteristics, which correspond to a maximum torque of 6 N.m and a maximal speed of 100 tr/min. For the 60 mm disk radius, the maximum tensile force is 100 N and maximum winding speed is 0.2π m/s (around 0.6 m/s). The motor characteristics are resumed in Table 2.

The robot requires a control cabinet to supply the motors.

2.6. The control cabinet

We need to control eight motors to follow a desired trajectory. The control cabinet is composed of classical industrial components. This architecture is similar to the IPanema robot family [58] or HRPCable [69]. The electrical control cabinet is composed of a Beckhoff CX5140-0155 embedded PC with an Intel®Atom™E3845 processor (1.91 GHz, 4 core). The computer programming is on TwinCAT 3 with the PLC language. The eight servomotors are controlled by four AX5206 digital servo drives from Beckhoff with two channels. The motor characteristics are resumed in Table 2 with a 400 VAC power supply. Absolute encoders multiturn SinCos Hiperface system Stegmann

SKM36S, SIL2 are embedded into the servomotors with an accuracy of ± 320 arc second (around $\pm 0.09^\circ$).

Setting the motors in motion to follow a trajectory requires the implementation of a control strategy.

3. Trajectory planning and calibration

This section develops the geometric models for the cable length control and the robot initial calibration.

3.1. Geometric model

In our application, thin cables are used. The geometric model can be simplified by neglecting the cable sagging due to their low linear mass (1.2 g/m). Thus, the cables are considered as rods of variable lengths with a low diameter and zero mass. The low diameter of the cable is taken into account for winding on the pulleys. These cables operate only under tension.

In this modeling approach, we only take into account the elasticity of the cables. We assume that the cables have a linear elastic behavior [17]. Their damping is assumed to be negligible. Indeed, damping has no influence on static stiffness. For the dynamic characterization, the modal properties (eigenfrequencies, modal deformations) are only slightly modified by the damping. This assumption allows an enormous simplification of the model and of the experimental characterization of the cable [16].

The geometric model of an RPC expresses the relationships between the cable length and the MPF pose. It must be carefully defined to reduce the geometric error.

3.1.1. Geometric model with additional pulleys

The geometric model with additional pulleys is well known and introduced by Tobias Bruckmann [18]. We detail these equations in this article, because they are part of the geometric model of the robot. The fixed frame of reference is $\mathcal{R}_0(O, \mathbf{e}_{x_0}, \mathbf{e}_{y_0}, \mathbf{e}_{z_0})$ and the MPF frame is $\mathcal{R}_E(C, \mathbf{e}_{x_E}, \mathbf{e}_{y_E}, \mathbf{e}_{z_E})$. Point O is defined at the center of the robot space and point C is the center of mass of the MPF. Points P_i and M_i are introduced as in Figure 13. Point P_i is a fixed point in the reference \mathcal{R}_0 which represents the cable entry point on the pulley. We introduce the pulley coordinate system $\mathcal{R}_{P_i}(P_i, \mathbf{e}_{x_i}, \mathbf{e}_{y_i}, \mathbf{e}_{z_i})$ fixed with respect to the frame. The unit vectors \mathbf{e}_{x_i} and \mathbf{e}_{y_i} are in the plane of rotation of the pulley and \mathbf{e}_{z_i} is carried by the axis of rotation of the pulley support. Using the rotation matrix \mathbf{R}_{0P_i} from the coordinate system \mathcal{R}_0 to the \mathcal{R}_{P_i} coordinate system, point B_i can therefore be projected into the reference \mathcal{R}_{P_i} such that:

$$\mathbf{p}_i \mathbf{b}_i^{Pi} = \mathbf{R}_{0P_i}(\mathbf{oc}^0 + \mathbf{R}_{0E} \mathbf{c}_i^E - \mathbf{op}_i^0) = \begin{bmatrix} x_{PB} \\ y_{PB} \\ z_{PB} \end{bmatrix} \quad (1)$$

The pulley support rotates with respect to the fixed frame \mathcal{R}_{P_i} of axis (P_i, \mathbf{e}_{z_i}) at an angle $\alpha_{pi} = (\widehat{\mathbf{e}_{x_i}, \mathbf{e}_{x_{2i}}})$ relative to the frame. We define a second coordinate system of the pulley $\mathcal{R}_{P_{2i}}(P_i, \mathbf{e}_{x_{2i}}, \mathbf{v}_i, \mathbf{e}_{z_i})$ such that $\mathbf{e}_{x_{2i}}$ is the projection of the vector $\mathbf{p}_i \mathbf{b}_i^{Pi}$ in the plane $(P_i, \mathbf{e}_{x_i}, \mathbf{e}_{y_i})$ and \mathbf{v}_i a vector orthogonal to \mathbf{e}_{z_i} and $\mathbf{e}_{x_{2i}}$.

Low speed (100 tr/min)		Nominal			Torque Max (N.m)	Inertia with brake (kg.mm ²)
Torque (N.m)	Current (A)	Torque (N.m)	Speed (tr/min)	Current (A)		
6	5.6	3.5	4500	3.3	18	440

Table 2: Motor characteristics.

The angle α_{pi} can be deduced by a trigonometric relation:

$$\alpha_{pi} = \arctan\left(\frac{y_{PB}}{x_{PB}}\right) \quad (2)$$

The rotation matrix of the reference $\mathcal{R}_{P_{2i}}$ with respect to the fixed reference \mathcal{R}_{P_i} is as follows:

$$\mathbf{R}_{P_{2i}P_i} = \begin{bmatrix} \cos(\alpha_{pi}) & -\sin(\alpha_{pi}) & 0 \\ \sin(\alpha_{pi}) & \cos(\alpha_{pi}) & 0 \\ 0 & 0 & 1 \end{bmatrix} \quad (3)$$

The position of the point M_i in the reference \mathcal{R}_{P_i} is therefore:

$$\mathbf{p}_i \mathbf{m}_i^{P_i} = \mathbf{R}_{P_{2i}P_i} \begin{bmatrix} r_{pi} \\ 0 \\ 0 \end{bmatrix} \quad (4)$$

The distance d_i between the points M_i and B_i is therefore equal to:

$$d_i = \|\mathbf{m}_i \mathbf{b}_i^{P_i}\|_2 = \|\mathbf{p}_i \mathbf{b}_i^{P_i} - \mathbf{p}_i \mathbf{m}_i^{P_i}\|_2 \quad (5)$$

If $r_p < d_i$, the winding angle β_{pi} can be calculated by the trigonometric relation:

$$\beta_{pi} = \pi - \beta_{1,i} - \beta_{2,i} = \pi - \arccos\left(\frac{z_{PB}}{d_i}\right) - \arcsin\left(\frac{r_p}{d_i}\right) \quad (6)$$

In the case where the intermediate pulleys are considered in the geometrical model, point A_i is not considered to be fixed on the frame (Figure 13). In addition, the cable length l_{pi} on the pulley depends on the MPF position [58]. This length is dependent on the radius r_{pi} (which corresponds to the sum of the radius of the pulley and the radius of the cable) and on its winding angle β_{pi} :

$$l_{pi} = r_{pi} \beta_{pi} \quad (7)$$

The position of point A_i is therefore:

$$\mathbf{p}_i \mathbf{a}_i^{P_i} = \mathbf{p}_i \mathbf{m}_i^{P_i} + \mathbf{R}_{P_{2i}P_i} \begin{bmatrix} -r_{pi} \cos(\beta_{pi}) \\ 0 \\ r_{pi} \sin(\beta_{pi}) \end{bmatrix} \quad (8)$$

The reference of cable $\mathcal{R}_{cable}(B_i, \mathbf{u}_i, \mathbf{v}_i, \mathbf{w}_i)$ is defined such that \mathbf{u}_i is as previously carried by the cable line:

$$\mathbf{u}_i^{P_i} = -\frac{\mathbf{a}_i \mathbf{b}_i^{P_i}}{\|\mathbf{a}_i \mathbf{b}_i^{P_i}\|_2} \quad (9)$$

\mathbf{w}_i is orthogonal to \mathbf{u}_i and \mathbf{v}_i .

The length between points A_i and B_i therefore gives:

$$l_i = \|\mathbf{a}_i \mathbf{b}_i^{P_i}\|_2 = \|\mathbf{p}_i \mathbf{b}_i^{P_i} - \mathbf{p}_i \mathbf{a}_i^{P_i}\|_2 \quad (10)$$

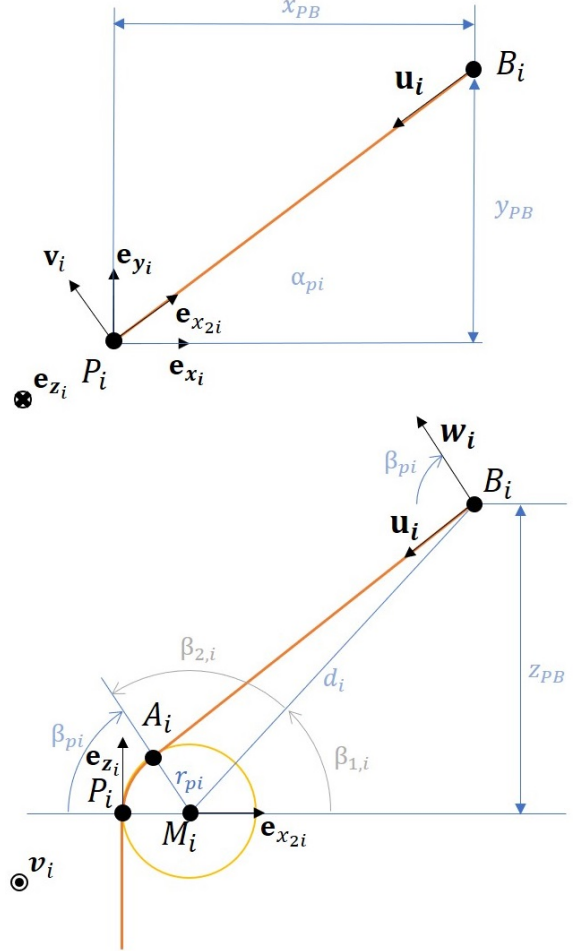


Figure 13: Pulley Schematic

The total cable length from point P_i to point B_i is therefore:

$$l_{robot} = r_{pi} \beta_{pi} + l_i \quad (11)$$

If r_{pi} is zero, \mathbf{oa}_i^0 is equal to \mathbf{op}_i^0 . The exit anchor point of the winch is also not fixed and depends on the motor angle.

3.1.2. Winch modeling

The main design contribution of this article is to propose a radial winding of the cable. The cable winding radius r_e varies according to the winding angle. The intermediate pulley and the disc are assumed to be in the same plane. Figure 14 represents the two possible winding configurations in the frame of pulley \mathcal{R}_{P_i} . Point B_i is the cable exit point on the winch. Point E_i is the center of the fixed motor axis in \mathcal{R}_0 and \mathcal{R}_{P_i} .

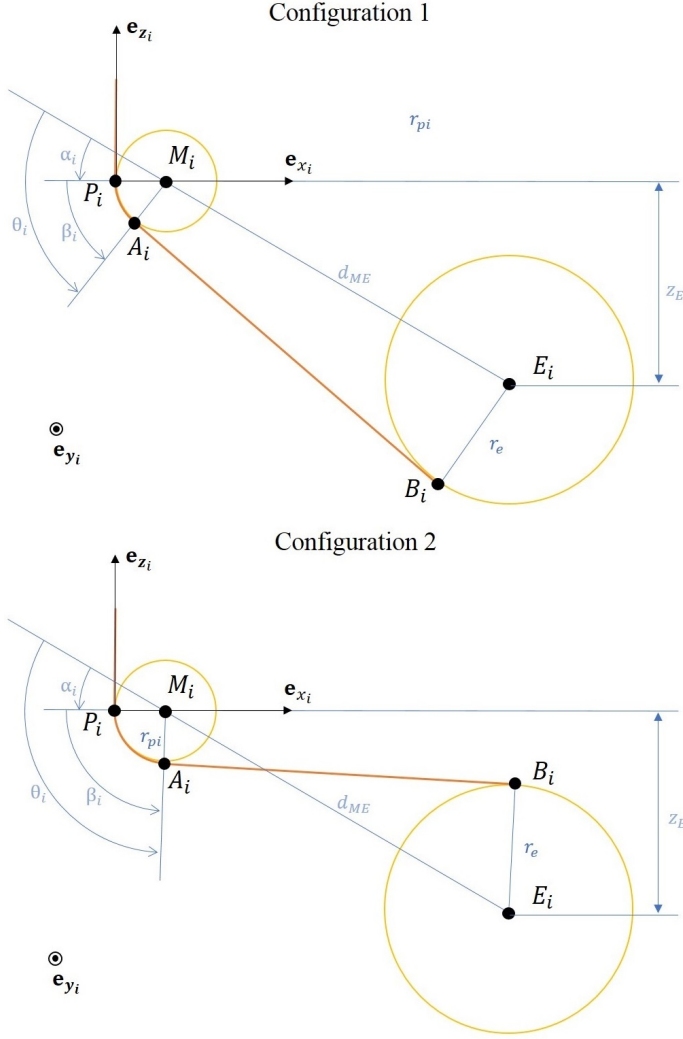


Figure 14: The two possible winding configurations.

The distance d_{ME} between points M_i and E_i is equal to:

$$d_{ME} = \|\mathbf{m}_i \mathbf{e}_i^{Pi}\|_2 \quad (12)$$

Depending on the winding configuration, the winding angle β_i of the small intermediate pulley can be obtained by two methods (as for the pulley-belt systems where the belt can be crossed). In the case of the first configuration β_i will be equal to:

$$\beta_i = \theta_i - \alpha_i = \frac{\pi}{2} - \arcsin\left(\frac{r_{pi} + r_e}{d_{ME}}\right) - \arcsin\left(\frac{z_E}{d_{ME}}\right) \quad (13)$$

In the case of the second configuration β_i will be equal to:

$$\beta_i = \theta_i - \alpha_i = \frac{\pi}{2} + \arcsin\left(\frac{r_{pi} + r_e}{d_{ME}}\right) - \arcsin\left(\frac{z_E}{d_{ME}}\right) \quad (14)$$

Point position A_i is calculated in a similar way to equation 8:

$$\mathbf{p}_i \mathbf{a}_i^{Pi} = \mathbf{p}_i \mathbf{m}_i^{Pi} - \begin{bmatrix} r_{pi} \cos(\beta_i) \\ 0 \\ r_{pi} \sin(\beta_i) \end{bmatrix} \quad (15)$$

Point position B_i will depend on the configuration. For the first configuration:

$$\mathbf{p}_i \mathbf{b}_i^{Pi} = \mathbf{p}_i \mathbf{e}_i^{Pi} - \begin{bmatrix} r_e \cos(\beta_i) \\ 0 \\ r_e \sin(\beta_i) \end{bmatrix} \quad (16)$$

And for the second configuration:

$$\mathbf{p}_i \mathbf{b}_i^{Pi} = \mathbf{p}_i \mathbf{e}_i^{Pi} + \begin{bmatrix} r_e \cos(\beta_i) \\ 0 \\ r_e \sin(\beta_i) \end{bmatrix} \quad (17)$$

The cable length at the winch can be calculated using equation 11. This length depends on the radius of the cable winding which makes the position of point B_i fluctuate.

$$l_{winch} = \|\mathbf{p}_i \mathbf{b}_i^{Pi} - \mathbf{p}_i \mathbf{a}_i^{Pi}\|_2 + r_{pi} \beta_i \quad (18)$$

3.1.3. Geometric model considering the elastic deformation of the cables

We may consider that the cable elasticity on the control loop can lower the MPF pose error as shown theoretically and experimentally by Sana Baklouti [70]. We consider the elastic deformation of the cable from the winch exit point to the MPF anchor point B_i . The total length from the winch to the platform is equal to:

$$l_{ti} = l_{winch} + l_{const} + l_{robot} \quad (19)$$

The length l_{const} is the fixed cable length between the two points P_i from the two intermediate pulleys.

For steel cables, the elastic deformation of the cables can be assumed to be linear [16]. So, the cable rigidity is given by:

$$k_i = \frac{ES}{l_{0,i}} \quad (20)$$

Where E is the cable elastic modulus, S is the cross area of the cable, and $l_{0,i}$ is the free length of the cable. So, the cable force t_i is given by:

$$t_i = \frac{ES}{l_{0,i}} (l_{ti} - l_{0,i}) \quad (21)$$

It is therefore possible to control the cable tension by modifying the free length:

$$l_{0,i} = \frac{ES}{t_i + ES} l_{ti} \quad (22)$$

The cable tension t_i can be determined with the help of the MPF static equilibrium [71]. The wrench of the forces applied by the cables on the MPF can be expressed as a function of the cable tensions t_i ($i = 1, \dots, 8$) on the MPF as follows:

$$\mathbf{w}_{cables}^0 = \begin{bmatrix} \mathbf{F}_{cables}^0 \\ \mathbf{M}_{cables}^0(C) \end{bmatrix} = \begin{bmatrix} \sum_{i=1}^8 t_i \mathbf{u}_i^0 \\ \sum_{i=1}^8 t_i \mathbf{u}_i^0 \times \mathbf{b}_i \mathbf{c}^0 \end{bmatrix} = \mathbf{J}^t \begin{bmatrix} t_1 \\ \vdots \\ t_8 \end{bmatrix} \quad (23)$$

where \mathbf{F}_{cables}^0 and $\mathbf{M}_{cables}^0(C)$ are respectively the force and moment applied by the cables at point C and expressed in the fixed

reference frame \mathcal{R}_0 . \mathbf{J}^t is the wrench matrix which is the transpose of the Jacobian matrix from the inverse kinematic model also expressed in \mathcal{R}_0 . It is given by:

$$\mathbf{J}^t = \begin{bmatrix} \mathbf{u}_1^0 & \cdots & \mathbf{u}_8^0 \\ \mathbf{u}_1^0 \times \mathbf{b}_1 \mathbf{c}^0 & \cdots & \mathbf{u}_8^0 \times \mathbf{b}_8 \mathbf{c}^0 \end{bmatrix} \quad (24)$$

Under static equilibrium conditions, the wrench of forces \mathbf{w}_{cables}^0 applied by the cables balances the torsor of external forces \mathbf{w}_{ext}^0 (force and torque) exerted on the MPF.

$$\mathbf{w}_{cables}^0 + \mathbf{w}_{ext}^0 = 0 \quad (25)$$

The following relation is obtained:

$$\begin{cases} \mathbf{J}^t \begin{bmatrix} t_1 \\ \vdots \\ t_8 \end{bmatrix} = \begin{bmatrix} \sum_{i=1}^8 t_i \mathbf{u}_i^0 \\ \sum_{i=1}^8 t_i \mathbf{u}_i^0 \times \mathbf{b}_i \mathbf{c}^0 \end{bmatrix} = - \begin{bmatrix} \mathbf{F}_{ext}^0 \\ \mathbf{M}_{ext}^0(C) \end{bmatrix} = -\mathbf{w}_{ext}^0 \\ t_{min} \leq t_i \leq t_{max} \end{cases} \quad (26)$$

Equation 26 gives an overdetermined system. There are an infinite number of possible solutions for cable tensions. A force distribution algorithm [72] with additional conditions may be used to find a cable tension solution that satisfies the equilibrium equation 26.

In the case of a redundant robot with 8 cables and 6 degrees of freedom, the Jacobian matrix is not square. The pseudo-inverse matrix \mathbf{J}^{+t} is therefore introduced.

$$\mathbf{t} = \begin{bmatrix} t_1 \\ \vdots \\ t_8 \end{bmatrix} = -\mathbf{J}^{+t} \mathbf{w}_{ext}^0 + \mathbf{H} \boldsymbol{\lambda} \quad (27)$$

The columns of the \mathbf{H} matrix (8×2 size) represent two linearly independent vectors of the kernel of the Jacobian matrix \mathbf{J}^t defined by the equation $\mathbf{J}^t \mathbf{H} = 0$. It is therefore necessary to find the multiplier vector of the kernel $\boldsymbol{\lambda}$ of size 2×1 . $\mathbf{t}_{kern} = \mathbf{H} \boldsymbol{\lambda}$ corresponding to an internal tension of the cables which will not disturb the balance of the forces on the MPF. This problem comes down to finding the solution to $\boldsymbol{\lambda}$ according to the defined optimization constraints and the equation :

$$\mathbf{t}_{min} + \mathbf{J}^{+t} \mathbf{w}_{ext}^0 \leq \mathbf{t}_{kern} \leq \mathbf{t}_{max} + \mathbf{J}^{+t} \mathbf{w}_{ext}^0 \quad (28)$$

Where \mathbf{t}_{min} and \mathbf{t}_{max} are two column vectors comprising the minimum and maximum loads of the cables. The potential solutions represent the intersection between the hypercube of size 8 and the hyperplane of dimension 2. If there is no intersection, this means that there is no solution. There are several algorithms to compute the solutions of the kernel according to different optimization criteria [71, 73, 72].

We have chosen to use the closed-loop force distribution algorithm proposed by Andreas Pott and Tobias Bruckmann in [72]; because it is simple to implement and does not require the use of an optimization function to determine the $\boldsymbol{\lambda}$ vector. The tensions solution is as follows:

$$\mathbf{t} = \mathbf{t}_m + \mathbf{t}_v \quad (29)$$

The algorithm proposes a choice of load between the minimum and maximum load of the cables. \mathbf{t}_m is calculated such that its components are equal to:

$$t_m = (t_{min} + t_{max}) / 2 \quad (30)$$

\mathbf{t}_v is calculated from the equilibrium equation 26 and the pseudo-inverse matrix \mathbf{J}^{+t} :

$$\mathbf{t}_v = -\mathbf{J}^{+t} (\mathbf{w}_{ext}^0 + \mathbf{J}^t \mathbf{t}_m) \quad (31)$$

The cable tensions are then checked to be within t_{min} and t_{max} . If t_i is less than t_{min} , then $t_i = t_{min}$. If t_i is greater than t_{max} , then $t_i = t_{max}$. In these particular cases, the tension no longer guarantees the stability of the system.

So with the help of the cable length geometric model 19 and the distribution force algorithm 29, it is possible to control the cable free length using equation 22.

3.2. Control

The cable length is controlled with the motor encoder output based on a standard machine tool control. This type of control is highly suitable as we wish to follow a trajectory with a pre-defined velocity using the motor encoder feedback. The contribution of this section lies in trajectory planning considering the variation of the winch radius and the elastic deformation of the cable on its whole unwound length.

3.2.1. Position/velocity/current control

The control is performed in the joint space. All the motors have the same position/velocity/current control law (Figure 15). The desired angles \mathbf{q}_{des} and the desired angular velocity $\dot{\mathbf{q}}_{des}$ are the instructions given to the controller. The servo drives provide the measured position \mathbf{q}_{mes} , velocity $\dot{\mathbf{q}}_{mes}$ and current \mathbf{i}_{mes} . The output electric voltages are noted \mathbf{u} .

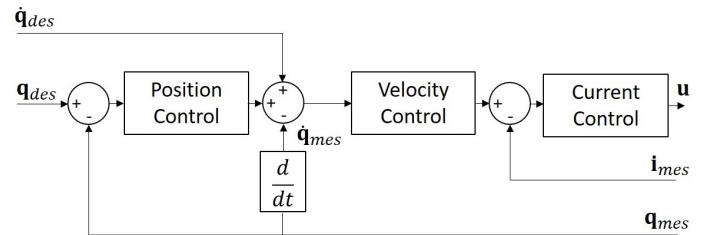


Figure 15: Position/velocity/current control

The position control is based on a proportional gain K_p . The velocity loop and current loop use a proportional-integral (PI) corrector, whose transfer function in the Laplace domain is:

$$G(s) = K \left(1 + \frac{1}{T \cdot s} \right) \quad (32)$$

Where K is the gain, T is the integral time and s is the Laplace variable. The velocity loop has a proportional gain K_v and an integral time T_v . The current loop has a proportional gain K_I and an integral time T_I . These values are set experimentally and are resumed in table 3.

The desired motors angles are determined using a trajectory generator and the robot inverse geometric model.

K_p	K_v	T_v	K_I	T_I
33.33 s^{-1}	0.480 A/(rad/s)	1 ms	40.6 V/A	0.8 ms

Table 3: Position/velocity/current control parameters.

3.2.2. Trajectory planning

The MPF position is interpolated by a 5-order polynomial function in order to control speed, acceleration and jerk. The experimental trajectory is a circle parametrized by a rotation angle. The interpolation is done on the rotation angle trajectory. So the desired MPF velocity is null at 0° and 360° and maximal at 180° . The trajectory generator returns the time-dependent desired MPF position \mathbf{x}_{des} . This planning is computed offline. Figure 16 shows the motor trajectory.

The computation of the motor trajectory is based on the geometric model of the CDPR. The function $\mathbf{l}_{init} = f(\mathbf{x}_{des})$ that computes the desired cable lengths regarding the desired MPF position \mathbf{x}_{des} is named "partial geometric model". As the "global geometric model" computes the desired angular positions \mathbf{q}_{des} of the motor regarding \mathbf{x}_{des} , two "partial geometric models" are compared and explained in Section 3.1, thus enabling the desired cable lengths \mathbf{l}_{des} to be determined. The first one considers only the length of the cables to be wound and unwound. The second one takes into account the cable elastic deformation as well as the cable load. The cable length variations $\Delta \mathbf{l}$ are obtained by subtracting the initial lengths \mathbf{l}_{init} of the cable at the beginning of the movement from the desired length \mathbf{l}_{des} . The initial lengths \mathbf{l}_{init} are determined using the initial platform position and the inverse geometric model. The angle variations $\Delta \theta$ are computed by dividing the length variations $\Delta \mathbf{l}$ by the winding radii \mathbf{r} of the disks. The algorithm for calculating the winding radii \mathbf{r} is presented in Section 3.3.2. The desired angular positions \mathbf{q}_{des} of the motors are obtained by adding the angle variations $\Delta \theta$ and the initial angles of the motors θ_{init} obtained using the absolute encoder measurements. The desired motor angular velocities $\dot{\mathbf{q}}_{des}$ are the time derivative of the desired angular positions \mathbf{q}_{des} .

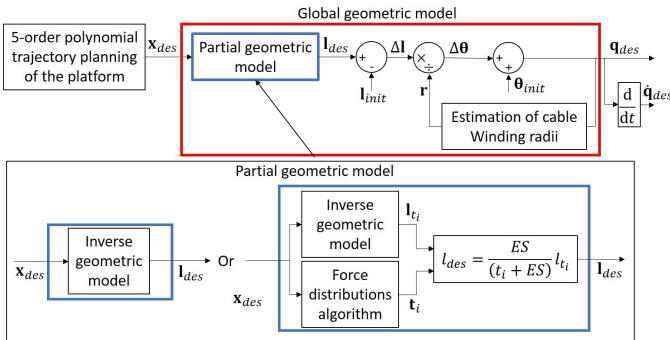


Figure 16: Angular trajectory generation of the motors.

A precise geometric model enables a reduction in the robot geometric error. However, in order to achieve this, an accurate system calibration is required to determine the robot initial parameters.

3.3. Calibration

Geometric calibration is performed using a laser tracker with an accuracy of $21 \mu\text{m}$ at 1 m. Six fixed points are physically located on the robot frame (represented by orange circles in Figure 1). These six points are used to compute the transformation between the measurement reference frame attached to the laser tracker and the robot frame reference frame. The geometric identification of our prototype consists in measuring the positions of the pulleys and the winches, including the determination of the exit and entry points of the cables on the pulleys. We will also determine the winding pattern of the cable on the disk.

3.3.1. Robot space measurement

To identify the geometric model with the pulley defined in Section 3.1, it is necessary to know the position of point P_i and the rotation matrix between the robot frame and the pulley fixed frame. During the assembly of the pulleys, an adapter is fixed to the pulley as shown in Figure 17 allowing to position the laser tracker ball reflector on the rotation axis of the pulley. The pulley vertical rotation is done manually. Several points forming a circle are measured using the laser tracker. Point P_i corresponds to the circle center and the first pulley rotation axis corresponds to the circle normal vector. The Matlab fit function [74] is used to determine the plane equation and the circle optimal equation passing through the measurement points by the Levenberg-Marquardt algorithm. The plane equation is used to determine the rotation matrix. The circle equation is used to determine point position P_i .

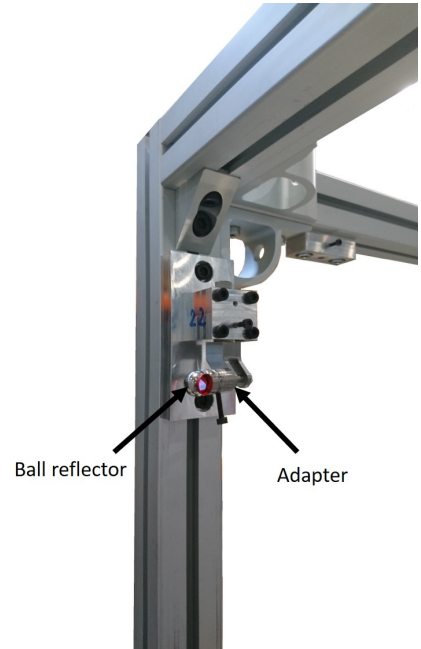


Figure 17: Pulley measurement position

The same method is used to determine the positions of the winch axes in the fixed base frame using 4 measurement points. The measurement points on the winch are shown in Figure 18.

During the measurement, the winch is at the 0° position of the absolute encoder. We can therefore determine the origin of the disk reference frame with respect to the robot reference frame.

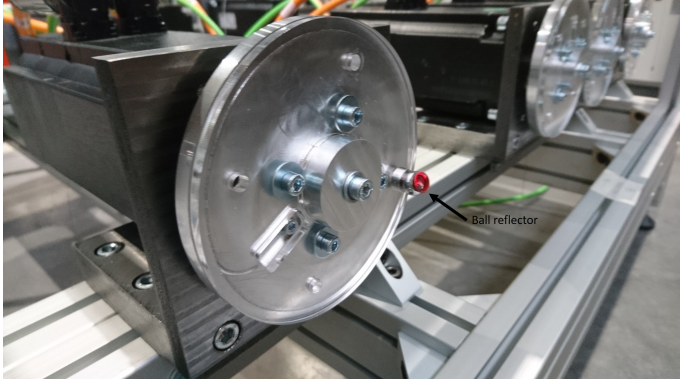


Figure 18: Winch measurement position

Once the winch position is established in the measurement frame and hence that of the robot, it is necessary to determine the cable winding variation on the disk.

3.3.2. Cable winding geometric identification

To identify the pattern of variation of the cable winding radius, an experimental characterization of the winding is set up. For each winch, the length wound onto the disk is measured. A Micro-Epsilon WPS-750-MK30-E draw-wire sensor with a resolution of 0.2 mm is used to measure the cable length output as a function of the motor angular position. Since the sensor stroke is 750 mm, the winding is divided into 3 phases 0° - 500° , 500° - 1000° and 1000° - 1500° . The motor stops every 5° . At each step, the length measurement of the draw-wire sensor is taken.

First, we consider that the winding of the cable is linear, i.e. the relation between the motor angle $\theta_{winding}$ and the output length $l_{winding}$ is the following:

$$l_{winding} = r_e \theta_{winding} \quad (33)$$

Where r_e is the winding radius of the cable and the motor angle $\theta_{winding}$ is expressed in radians. The winding radius of layer 0 is 60 mm plus the cable radius (0.27 mm). The length error between equation 33 and the experimental length is shown in Figure 19. We can see that the error increased with the winch angle. By looking closely at the blue and red lines of the layer number on the winch, we can observe several slope changes of this error which are repeated every 360° . These slope changes are caused by the cable overlap. The offset angle is different for each winch, depending on the position of the motors and the 0 value of the absolute encoders.

For each winch, we identify the angle when the cable overlaps. The angle at which the shift occurs is determined on the CAD model of the winches. To prevent the radius change from being too abrupt for the controller, the radius shift occurs linearly over a range of 8.76° . The angles at the beginning of the shift θ_{start} and the end of the shift θ_{end} are noted in Table 4. The

algorithm for calculating the winding radius as a function of the winding angle is as follows:

Algorithm 1 The algorithm for calculating the winding radius

Input: $\theta_{winding}$, θ_{start} , θ_{end} , n , nb_{cables}

Output: r_e

```

1: for  $i = 1$  to  $nb_{cables}$  do
2:   if  $\theta_{start}(i) + 2\pi n \leq \theta_{winding}(i) \leq \theta_{end}(i) + 2\pi n$  then
3:      $r_e(i) = \frac{d_{cable}}{\theta_{end}(i) - \theta_{start}(i)} (\theta_{winding} - (\theta_{start}(i) + 2\pi n)) +$ 
        $r_{init} + d_{cable}n$ 
4:   else
5:      $r_e(i) = r_{init} + d_{cable}n$ 
6:   end if
7: end for

```

The cable length error with winding radius variation is represented in Figure 20. This gives rise to more accurate cable length prediction. There are still errors which are caused by the uncertainty of the winding layer radii on winches 2,4 and 5. But for the other winches, these errors are of the same order of magnitude as the draw-wire sensor resolution (0.2 mm). For the experimental prototype, we will use the theoretical layer radii.

The geometrical model considers this variation for the calculation of the robot trajectories ("Cable winding radii estimation" block from Figure 16). For our geometric model, considering the cable elastic deformation, it is necessary to determine the cable initial preload.

3.3.3. Static force determination

The influence of the initial preload in the cables is analyzed for the two platforms. Three levels of preload are studied and summarized in Table 5. These initial preloads are set up using motor torque feedback from current measurement. They were chosen by increasing or decreasing the angles of the motors, that modify the cables free length. The position of the platform is naturally slightly modified. The initial platform position is measured yet again using the laser tracker for each new preload. The initial cable forces are estimated by measuring the motor torque divided by the theoretical radius of winding estimated by the geometric model of the winch.

First, we will determine the cable forces calculation reliability from the motor torques. To this end, we check if the static equilibrium equation (equation 26) of the platform is verified with the estimated cable forces (table 5). Table 6 summarizes the force of the cables projected into the robot frame.

We find that the force is mainly along F_z as it should balance the weight of the platform. The experimental force estimated according to F_z is approximately 2.5 N above the theoretical force for the 6 preload levels. This difference may be due to a slight overestimation of the torque. Weak forces along F_x and F_y are also present. The sum of the moments of the cables is almost zero. In addition to the measurement error of the motor torque, the accumulation of small geometric errors may be sufficient to explain this difference, for example:

- platform center of gravity position error;

Winch	1	2	3	4	5	6	7	8
θ_{start} (deg)	136.58	61.75	234.92	242.91	385.11	363.99	206.10	301.61
θ_{end} (deg)	145.34	70.5	243.68	251.67	393.87	372.75	214.86	310.37

Table 4: Layer offset angle.

	Init X			Optim		
	Level 1	Level 2	Level 3	Level 1	Level 2	Level 3
Cable 1	12.55	14.27	18.99	17.61	20.60	22.68
Cable 2	16.41	18.04	22.22	15.57	17.42	22.37
Cable 3	10.65	12.49	15.02	14.91	17.90	18.48
Cable 4	14.41	14.87	19.13	12.80	13.03	16.71
Cable 5	5.44	7.75	15.34	11.20	14.54	19.83
Cable 6	11.15	14.14	20.59	13.57	17.94	23.24
Cable 7	2.05	4.12	9.53	6.08	8.50	12.64
Cable 8	6.75	8.24	12.62	6.17	9.39	12.39
Mean	9.93	11.74	16.68	12.24	14.92	18.54

Table 5: Initial preload levels in N in the cables estimated using the motor torque.

		F_x (N)	F_y (N)	F_z (N)	M_x (N.m)	M_y (N.m)	M_z (N.m)
Init X	Theoretical	0	0	25.49	0	0	0
	Level 1	-0.04	1.35	27.94	-0.04	0.12	-0.01
	Level 2	0.37	2.72	27.74	-0.04	0.14	-0.01
	Level 3	0.67	1.49	27.63	-0.12	0.19	-0.04
Optim	Theoretical	0	0	25.16	0	0	0
	Level 1	0.59	1.62	28.10	-0.05	0.15	0.02
	Level 2	0.48	2.56	27.74	0.01	0.17	0.08
	Level 3	1.08	3.27	27.71	0.00	0.18	0.15

Table 6: Force sum in the cables projected in the robot frame.

- error in identifying the actual direction of the cables;
- error in identifying anchor points;
- straight line of the cable not in the plane of rotation of the intermediate pulley;
- winch radius estimation error.

Despite these errors, estimating the force in the cables through the motor torque is a viable solution to calculate the static forces of the cables before the start of the trajectory. The preload is not controlled during the trajectory, but initializing the preload using encoder measurement may be sufficient to avoid slack cables.

The calibration and the geometric model are taken into account to generate the robot trajectory. The next section will show the MPF geometric error for a desired trajectory.

4. Performance

This section analyzes the performance of the prototype. In order to observe the benefits in terms of dynamic performance with a platform optimizing the stiffness of the robot, the two platforms (Init X and Optim) previously introduced are studied

in [15, 16]. In these previous articles, we have seen the configuration of the cables have an influence on the robot stiffness. Using a prototype without motors and a modal analysis, we saw that the vibration frequencies of the optim platform were higher than those of the init X platform. We also observed that it was possible to increase the vibration frequencies of the MPF by increasing the preloads of the cables. In this section, we will observe if these results are also valid for a movement of the mobile platform on a large trajectory. We will also observe the performance gain by considering the elasticity of the cables in the path generation.

4.1. Robot setting-up

For the assembly of the platform to the robot, the platform is first attached to the frame by means of aluminum profiles. The cables are routed through the platform intermediate pulleys to the cable reel. The angle of the reels is 0° . The cable is then positioned on its layer 0 and attached to the reel with a screw (see Figure 7). The transparent side is repositioned. The cables are then stretched by winding the cables on the discs. The platform is then detached from the profile. The platform position is then measured with the laser tracker. The laser tracker makes it possible to determine the position and the initial orientation of the platform. For the Optim MPF, the anchor points are in

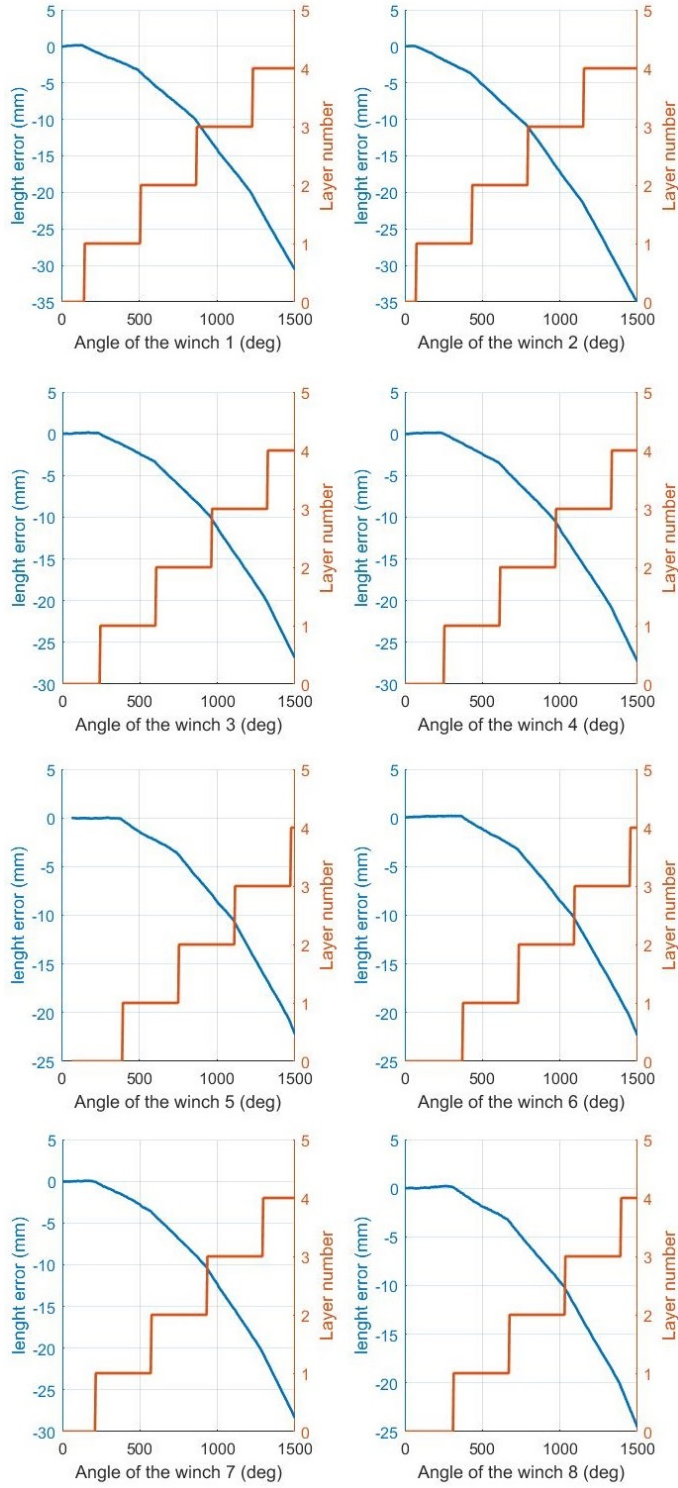


Figure 19: Length error with continuous winding radius (blue line) and the layer number (red line) as a function of the winch angle.

the same plane and only points 2, 3 and 4 are necessary to measure the initial pose configuration. For the Init X platform, the anchor points are in two planes, which requires 6 measurement points (points 2, 3, 4 in downward and upward). These planes are in reality not parallel and their positions and orientations in

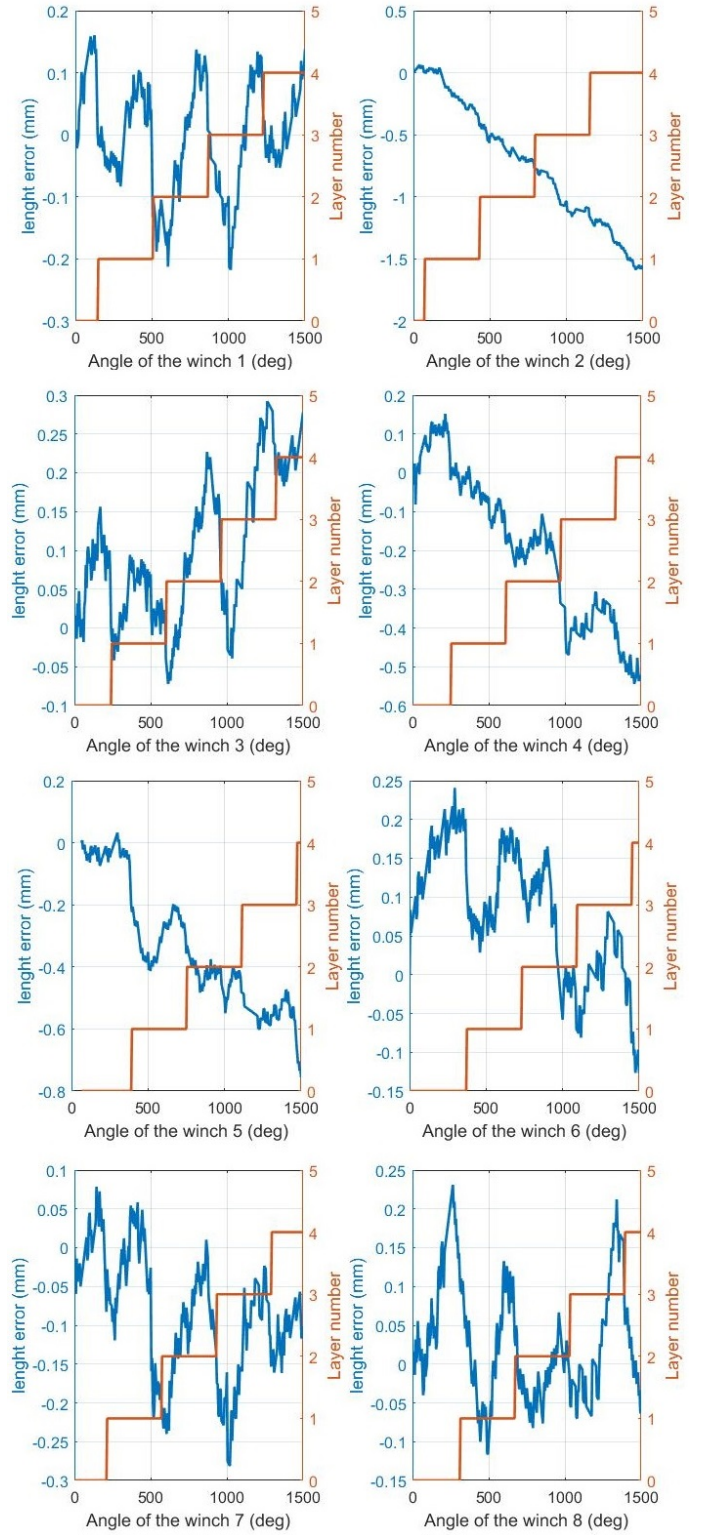


Figure 20: Length error with winding radius variation (blue line) and the layer number (red line) as a function of the winch angle.

the MPF frame are not accurate. By measuring the position of these two planes, it is possible to determine the anchor point position on the platform. With these experimental measurements, we reduce the MPF geometric error. The positions of the sights

on the two platforms are visible in Figures 21 and 22. Using the controller, the platform is then moved to the initial path position, ie (0.1 m 0 m -0.2 m). The origin of the frame is located in the center of the workspace.

The test path is a circle with 0.1 m radius and placed at a height of -0.2 m. The trajectory time is 6.28 s (2π). The platforms are moved using the position control (see Section 3.2.1). This trajectory is inside the robot printing space. The MPF position is measured using the laser tracker with an acquisition frequency of 200 Hz. Only the Cartesian position (x, y, z) of the ball is measured in point 1. We will also observe the influence of the preload in the cables. The initial preloads in the cables for the two platforms are shown in table 5. First, we study the geometric error without considering the cable elastic deformation. Then, we will observe the improvement by adding the cable elastic deformation in the geometric model.

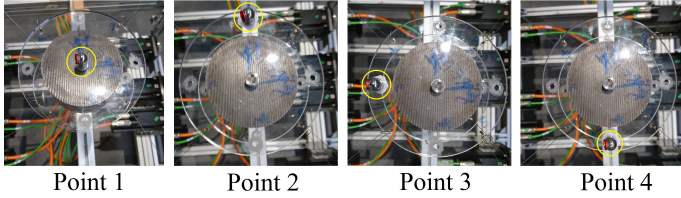


Figure 21: Laser sight position on the Init X platform.

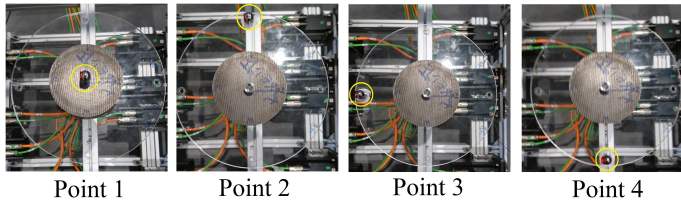


Figure 22: Laser sight position on the Optim platform.

4.2. Geometric error without considering the cable elastic deformation

In this analysis, only the geometric error of point 1 of the two platforms is analyzed. Point 1 of the Init X platform is 3 mm higher than point 1 of the Optim platform. The positions of these points on the platforms are therefore close. We do not consider the time delay between the desired trajectory and the experimental trajectory. Figure 23 shows the height error and the circular error of the Init X platform. Figure 24 shows the height error and the circular error of the Optim platform. The minimum, maximum and root mean square errors are summarized in Table 7.

For the Init X platform, the height error increases with the preload. At preload level 3, the root mean square (RMS) error at z is 61 μm . The preload increased the circular geometric error of the platform, and modified the center of the trajectory. This may be due to the geometric model of the control which does not consider the deformation of the cables by preload. The maximum circular error is less than 1mm and the circular RMS error is less than 0.3 mm.

		Circular (μm)			Height (μm)		
		Min	Max	RMS	Min	Max	RMS
Init X	Level 1	-248	680	235	-104	100	27
	Level 2	-229	535	202	-135	85	40
	Level 3	-103	847	290	-167	89	61
Optim	Level 1	-1097	110	461	-150	87	61
	Level 2	-1727	135	788	-167	74	65
	Level 3	-1400	190	611	-165	63	69

Table 7: Circular and height errors for both platforms and the 3 preload levels at points 1.

In Figure 23, we can distinguish a shift of the error at 2 s and 3.3 s, either around 70° and 200.5° on the circular error. This shift is due to a change in the cable winding radius on disc 7. It is therefore possible to improve the transition between the cable winding layers in the geometric model to eliminate this shift which increases the geometric error. In our geometric model, the transition is abrupt between the layers, but it seems to be smoother.

For the Optim platform, the circular RMS error is 788 μm and the RMS error according to z is 65 μm at the level 2 preload. As before, there is a winding layer change on disk 7. This shift takes place at 1.5 s and 3.5 s. There are also winding layer changes for disks 1 and 6, but these changes are less visible in the Figures. The circular geometric error is mainly negative, possible due to a greater preload in the cables that shift the center of the circle trajectory.

The circular geometric error of the Init X platform is lower than that of the Optim platform. The altitude error is less than 0.2mm for both platforms. The circular error of the Init X platform is less than 1 mm. It is between 1 mm and 2 mm for the Optim platform with slightly higher levels of preload in the cables (see Table 5). There is also more layer change on the discs with the Optim platform which increases the geometric error.

From authors' previous works [15, 16], the rotation rigidity of the Optim platform is better than the Init X platform. For translation rigidity no significant change was observed, because this rigidity depends mainly on the axial rigidity of the cables. We also saw that the rigidity of the Init X platform can greatly improve by increasing the cables tension. With the Fourier transform of the error, the spectral amplitude of the oscillations is represented in Figures 25 and 26. It can be observed that the amplitude of the oscillation with a frequency below 13 Hz are higher on the Init X platform on x and y than on the Optim platform. The movement of these low frequency oscillations is mainly rotation around the x axis and y axis. For both MPF, the translation oscillations are quite similar between 14 Hz and 18 Hz. From Figures 25, we can see that the amplitude of the low frequency oscillations can decreased by increasing the cable preload, and also increased the frequency of the oscillation. These results validate modal analysis from [16] with a dynamic trajectory. Note that, if we have chosen another measurement point far away from the MPF center (for example point 2), the amplitude oscillations will be more important.

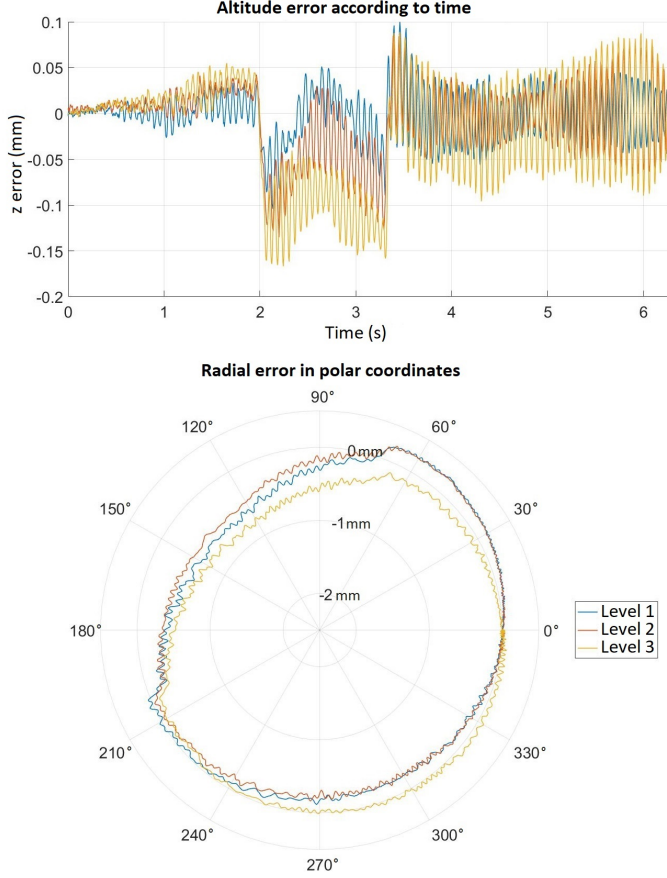


Figure 23: Height error and radial error for the Init X platform.

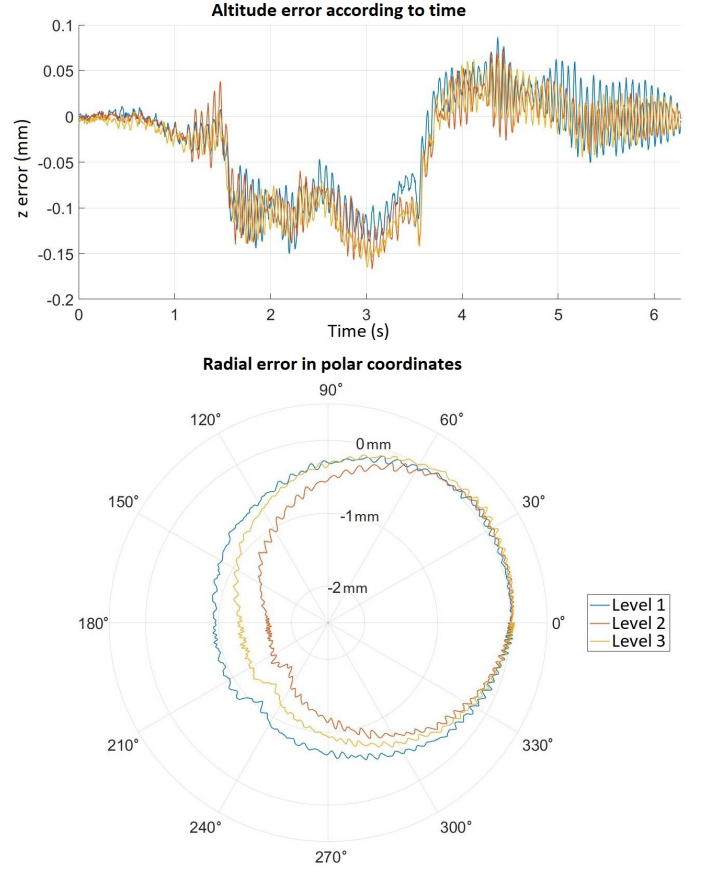


Figure 24: Height error and radial error for the Optim platform.

4.3. Geometric error considering the cable elastic deformation

We have seen previously that the preload causes an elastic deformation of the cable which increases the geometric error of trajectory following. To reduce this error, we will add this elastic deformation to the generation of trajectories. The partial geometric model is therefore modified as shown in Figure 16. To control the preload in the cables, we add a force distribution algorithm. The preload in the cables is initialized thanks to the feedback of the measurements of the motor torque, of the winch angle and the position of the platform using the laser tracker. Performance is evaluated on the Optim platform.

Figure 27 shows the height error and the circular error with and without the control of the cable deformation. Considering the cable elastic deformation in the generation of the trajectory enables a reduction in the geometric error. The maximum absolute height error is reduced from 0.15 mm to 0.1 mm. The maximum radial absolute error is reduced from 1 mm to 0.33 mm.

5. Conclusion

The design process and the implementation of a new CDPR has been presented in this paper. The proposed design uses a radial cable winding system rarely studied in the literature. The reel used in this experiment exhibits a non-linear variation

in radius between the different overlapping layers of the cable which has been taken into account in the geometric model.

It has been noted that the cable initial force estimation in static equilibrium is possible thanks to motor torque measurement on the prototype. The sum of cable forces is close to the platform static equilibrium conditions. Therefore, it does not seem useful to add an additional force sensor to measure the force of the cables in order to estimate the preload when the robot is not moving. However, it is necessary to study whether the dynamic force of the cable can also be calculated from the motor torque in a future work.

The radial error on the circular trajectory has been analyzed for two designs of the MPF. For both platforms, the geometric parameter uncertainties are the main source of errors on the robot path following. The abrupt variation in the reel radius creates a visible shift in the geometric error of the platform. It is therefore necessary to improve the winding layer modeling to reduce the error. Depending on the initial cable preload, the geometric error may decrease or increase.

Adding the cable elastic deformation caused by the preload in the path generation leads to a decreased in the geometric error. With the Optim platform, the geometric error is lower than 0.4 mm. These results make it possible to consider printing parts of acceptable quality with tolerances greater than 0.4 mm. However, there remains considerable room for improvement as

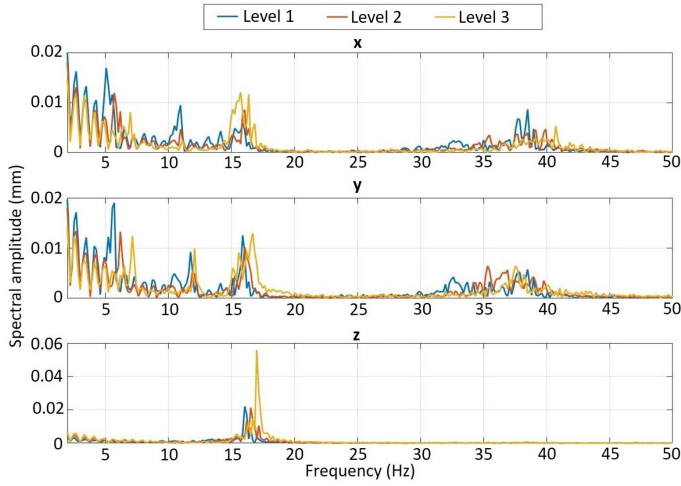


Figure 25: Amplitude plots of the Fourier transform of the errors measured in x , y , z at 0.1 m/s at point 1 of the Init X platform.

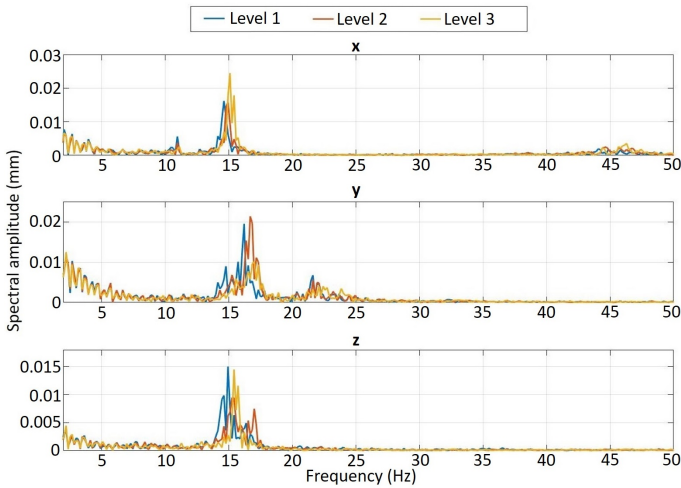


Figure 26: Amplitude plots of the Fourier transform of the errors measured in x , y , z at 0.1 m/s at point 1 of the Optim platform.

far as increasing the geometric performance of the proposed robot is concerned. In addition to characterizing the precision of the robot in the overall printing space, future work will add a 3d printer extruder to the mobile platform.

To improve the trajectory tracking of the prototype, it is essential to reduce the platform geometric error. The platform geometric error can be further reduced by improving the identification of the robot geometric parameters. The winch modeling can be improved so that the platform error caused by the radius variation is zero. Some robots also use compensation terms to reduce repeatable geometric errors. These terms can be optimized using machine learning methods. It is also possible to propose a second design of the disk with a spiral winding to avoid abrupt changes in radius. If this solution were adopted, the radius would no longer be constant, but would vary linearly with the winding angle.

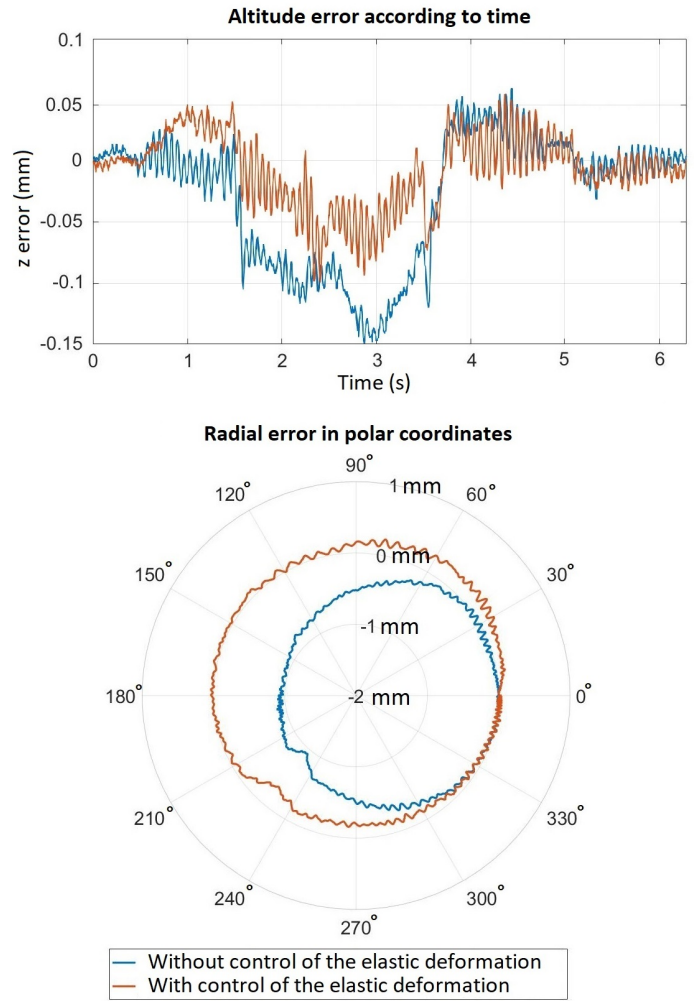


Figure 27: Error according to z and radial error for the Optim platform.

CRedit authorship contribution statement

Damien Gueners: Conceptualization, Methodology, Software, Validation, Investigation, Visualization, Writing - original draft. **Hélène Chanal:** Conceptualization, Supervision, Writing - review & editing. **Belhassen-Chedli Bouzgarrou:** Conceptualization, Supervision, Writing - review & editing.

Declaration of Competing Interest

The authors declare no conflict of interest.

Funding

This work is part of the CABFAB project funded by the Auvergne-Rhône-Alpes region as part of the 2017 Research Ambition Pack program.

Acknowledgment

We acknowledge S.mart network for their financial support for experimental validation. We acknowledge Wide Open to the

World (WOW!) program for their financial support that enables Damien Gueners to travel to Stuttgart. Damien Gueners thanks the Fraunhofer IPA institute in Stuttgart, in particular Marc Fabritius and Christopher Martin, for having welcomed him and allowed him to share and discuss for 2 months on CDPR applications. Damien Gueners thanks the SIGMA Clermont students, in particular Camila Borges Santos, for their contributions to the CABFAB project.

References

- [1] A. Pott, *Cable-driven parallel robots: theory and application*. Springer, 2018, vol. 120. [Online]. Available: <https://doi.org/10.1007/978-3-319-76138-1>
- [2] D. Q. Nguyen, M. Gouttefarde, O. Company, and F. Pierrot, "On the simplifications of cable model in static analysis of large-dimension cable-driven parallel robots," in *2013 IEEE/RSJ International Conference on Intelligent Robots and Systems*, 2013, pp. 928–934. [Online]. Available: <https://doi.org/10.1109/IROS.2013.6696461>
- [3] A. Pott, H. Mütterich, W. Kraus, V. Schmidt, P. Miermeister, and A. Verl, "IPAnema: A family of Cable-Driven Parallel Robots for Industrial Applications," in *Cable-Driven Parallel Robots*, T. Bruckmann and A. Pott, Eds. Berlin, Heidelberg: Springer Berlin Heidelberg, 2013, pp. 119–134. [Online]. Available: https://doi.org/10.1007/978-3-642-31988-4_8
- [4] T. Bruckmann, W. Lalo, K. Nguyen, and B. Salah, "Development of a Storage Retrieval Machine for High Racks Using a Wire Robot," in *Volume 4: 36th Mechanisms and Robotics Conference, Parts A and B*. American Society of Mechanical Engineers, aug 2012, pp. 771–780. [Online]. Available: <https://doi.org/10.1115/DETC2012-70389>
- [5] S. Qian, K. Bao, B. Zi, and N. Wang, "Kinematic Calibration of a Cable-Driven Parallel Robot for 3D Printing," *Sensors*, vol. 18, no. 9, p. 2898, 2018. [Online]. Available: <https://doi.org/10.3390/s18092898>
- [6] D. Surdilovic, J. Zhang, and R. Bernhardt, "STRING-MAN: Wire-robot technology for safe, flexible and human-friendly gait rehabilitation BT - IEEE 10th International Conference on Rehabilitation Robotics, ICORR 2007," no. c, pp. 446–453, 2007. [Online]. Available: <https://doi.org/10.1109/ICORR.2007.4428463>
- [7] P. Bosscher, R. L. Williams, and M. Tummino, "A Concept for Rapidly-Deployable Cable Robot Search and Rescue Systems," *Volume 7: 29th Mechanisms and Robotics Conference, Parts A and B*, pp. 589–598, 2005. [Online]. Available: <https://doi.org/10.1115/DETC2005-84324>
- [8] P. D. Campbell, P. L. Swaim, and C. J. Thompson, "Charlotte™ robot technology for space and terrestrial applications," *SAE Technical Papers*, 1995. [Online]. Available: <https://doi.org/10.4271/951520>
- [9] S. Kawamura and K. Ito, "A new type of master robot for teleoperation using a radial wire drive system," in *Proceedings of 1993 IEEE/RSJ International Conference on Intelligent Robots and Systems (IROS '93)*, vol. 1, 1993, pp. 55–60 vol.1. [Online]. Available: <https://doi.org/10.1109/IROS.1993.583079>
- [10] T. Dallej, M. Gouttefarde, N. Andreff, P.-E. Hervé, and P. Martinet, "Modeling and vision-based control of large-dimension cable-driven parallel robots using a multiple-camera setup," *Mechatronics*, vol. 61, pp. 20–36, 2019. [Online]. Available: <https://doi.org/10.1016/j.mechatronics.2019.05.004>
- [11] H. An, Y. Zhang, H. Yuan, W. Xu, and X. Wang, "Design Control and Performance of a Cable-Driving Module With External Encoder and Force Sensor for Cable-Driven Parallel Robots," *Journal of Mechanisms and Robotics*, vol. 14, no. 1, 08 2021, 014502. [Online]. Available: <https://doi.org/10.1115/1.4051608>
- [12] M. Hiller, S. Fang, S. Mielczarek, R. Verhoeven, and D. Franitza, "Design, analysis and realization of tendon-based parallel manipulators," *Mechanism and Machine Theory*, vol. 40, no. 4, pp. 429–445, 2005. [Online]. Available: <https://doi.org/10.1016/j.mechmachtheory.2004.08.002>
- [13] A. Pott, P. Tempel, A. Verl, and F. Wulle, "Design, implementation and long-term running experiences of the cable-driven parallel robot caro printer," in *Cable-Driven Parallel Robots*, ser. Mechanisms and Machine Science, A. Pott and T. Bruckmann, Eds. Cham: Springer, 2019, pp. 379–390. [Online]. Available: https://doi.org/10.1007/978-3-030-20751-9_32
- [14] D. Gueners, B. Chedli Bouzgarrou, and H. Chanal, "Static and dynamic analysis of a 6 DoF totally constrained cable robot with 8 preloaded cables," in *Cable-Driven Parallel Robots (CableCon 2019), Mechanisms and Machine Science*, A. Pott and T. Bruckmann, Eds. Springer, Cham, 2019, vol. 74, pp. 307–318. [Online]. Available: https://doi.org/10.1007/978-3-030-20751-9_26
- [15] D. Gueners, H. Chanal, and B. C. Bouzgarrou, "Stiffness optimization of a cable driven parallel robot for additive manufacturing," in *2020 IEEE International Conference on Robotics and Automation (ICRA)*, 2020, pp. 843–849. [Online]. Available: <https://doi.org/10.1109/ICRA40945.2020.9197368>
- [16] D. Gueners, B.-C. Bouzgarrou, and H. Chanal, "Cable Behavior Influence on Cable-Driven Parallel Robots Vibrations: Experimental Characterization and Simulation," *Journal of Mechanisms and Robotics*, vol. 13, no. 4, 04 2021, 041003. [Online]. Available: <https://doi.org/10.1115/1.4049978>
- [17] S. Behzadipour and A. Khajepour, "Stiffness of Cable-based Parallel Manipulators With Application to Stability Analysis," *Journal of Mechanical Design*, vol. 128, no. 1, p. 303, 2006. [Online]. Available: <https://doi.org/10.1115/1.2114890>
- [18] T. Bruckmann, L. Mikelsons, T. Brandt, M. Hiller, and D. Schramm, "Wire Robots Part I: Kinematics, Analysis & Design," in *Parallel Manipulators, New Developments*. I-Tech Education and Publishing, apr 2008, vol. 1, no. April. [Online]. Available: <https://doi.org/10.5772/5365>
- [19] M. Miyasaka, M. Haghighipناه, Y. Li, and B. Hannaford, "Hysteresis model of longitudinally loaded cable for cable driven robots and identification of the parameters," *Proceedings - IEEE International Conference on Robotics and Automation (ICRA)*, vol. 2016-June, pp. 4051–4057, 2016. [Online]. Available: <https://doi.org/10.1109/ICRA.2016.7487596>
- [20] S. Baklouti, E. Courteille, S. Caro, and M. Dkhil, "Dynamic and Oscillatory Motions of Cable-Driven Parallel Robots Based on a Nonlinear Cable Tension Model," *Journal of Mechanisms and Robotics*, vol. 9, no. 6, p. 061014, 2017. [Online]. Available: <https://doi.org/10.1115/1.4038068>
- [21] S.-H. Choi and K.-S. Park, "Integrated and nonlinear dynamic model of a polymer cable for low-speed cable-driven parallel robots," *Microsystem Technologies*, no. 24, pp. 4677–4687, 2018. [Online]. Available: <https://doi.org/10.1007/s00542-018-3820-7>
- [22] P. Tempel, F. Trautwein, and A. Pott, "Experimental Identification of Stress-Strain Material Models of UHMWPE Fiber Cables for Improving Cable Tension Control Strategies," in *Advances in Robot Kinematics 2018. ARK 2018. Springer Proceedings in Advanced Robotics*, vol. 8. Springer, Cham, 2019, no. January, pp. 258–265. [Online]. Available: https://doi.org/10.1007/978-3-319-93188-3_30
- [23] M. Wehr, A. Pott, and K. H. Wehking, "Bending fatigue strength and lifetime of fiber ropes," in *Mechanisms and Machine Science (Cable Con 2017)*, 2018, vol. 53, pp. 73–84. [Online]. Available: https://doi.org/10.1007/978-3-319-61431-1_7
- [24] V. Schmidt and A. Pott, "Bending cycles and cable properties of polymer fiber cables for fully constrained cable-driven parallel robots," in *Cable-Driven Parallel Robots (Cable Con 2017), Mechanisms and Machine Science*, C. Gosselin, P. Cardou, T. Bruckmann, and A. Pott, Eds. Springer, Cham, 2018, vol. 53, pp. 85–94. [Online]. Available: https://doi.org/10.1007/978-3-319-61431-1_8
- [25] J. P. Merlet and D. Daney, "A portable, modular parallel wire crane for rescue operations," *Proceedings - IEEE International Conference on Robotics and Automation*, pp. 2834–2839, 2010. [Online]. Available: <https://doi.org/10.1109/ROBOT.2010.5509299>
- [26] E. Ottaviano, M. Ceccarelli, and M. De Ciantis, "A 4-4 cable-based parallel manipulator for an application in hospital environment," in *2007 Mediterranean Conference on Control Automation*, 2007, pp. 1–6. [Online]. Available: <https://doi.org/10.1109/MED.2007.4433839>
- [27] E. Barnett and C. Gosselin, "Large-scale 3D printing with a cable-suspended robot," *Additive Manufacturing*, vol. 7, pp. 27–44, 2015. [Online]. Available: <https://doi.org/10.1016/j.addma.2015.05.001>
- [28] J.-P. Merlet, "Direct Kinematics of CDPR with Extra Cable Orientation Sensors: The 2 and 3 Cables Case with Perfect Measurement and Ideal or Elastic Cables," in *Cable-Driven Parallel Robots*, C. Gosselin, P. Cardou, T. Bruckmann, and A. Pott, Eds. Cham: Springer International Publishing, 2018, pp. 180–191. [Online]. Available:

- https://doi.org/10.1007/978-3-319-61431-1_16
- [29] A. Alikhani, S. Behzadipour, A. Alasty, and S. a. sadough vanini, "Design of a large-scale cable-driven robot with translational motion," *Robotics and Computer-Integrated Manufacturing*, vol. 27, pp. 357–366, 04 2011. [Online]. Available: <https://doi.org/10.1016/j.rcim.2010.07.019>
 - [30] J. B. Izard, M. Gouttefarde, C. Baradat, D. Culla, and D. Sallé, "Integration of a parallel cable-driven robot on an existing building façade," *Mechanisms and Machine Science*, vol. 12, pp. 149–164, 2013. [Online]. Available: https://doi.org/10.1007/978-3-642-31988-4_10
 - [31] M. Korayem, M. Bamdad, H. Tourajizadeh, H. Shafiee, R. Zehatab, and A. Iranpour, "Development of icasbot: a cable-suspended robot's with six dof," *Arabian Journal for Science and Engineering*, vol. 38, no. 5, pp. 1131–1149, 2013. [Online]. Available: <https://doi.org/10.1007/s13369-012-0352-9>
 - [32] A. Dubor, J.-B. Izard, E. Cabay, A. Sollazzo, A. Markopoulou, and M. Rodriguez, "On-site robotics for sustainable construction," in *Robotic Fabrication in Architecture, Art and Design 2018*, J. Willmann, P. Block, M. Hutter, K. Byrne, and T. Schork, Eds. Cham: Springer International Publishing, 2019, pp. 390–401. [Online]. Available: https://doi.org/10.1007/978-3-319-92294-2_30
 - [33] Y. Wu, H. H. Cheng, A. Fingrut, K. Crolla, Y. Yam, and D. Lau, "CU-brick cable-driven robot for automated construction of complex brick structures: From simulation to hardware realisation," in *2018 IEEE International Conference on Simulation, Modeling, and Programming for Autonomous Robots (SIMPAR)*. IEEE, may 2018, pp. 166–173. [Online]. Available: <https://doi.org/10.1109/SIMPAR.2018.8376287>
 - [34] L. Gagliardini, M. Gouttefarde, and S. Caro, *Design of Reconfigurable Cable-Driven Parallel Robots*. Cham: Springer International Publishing, 2018, pp. 85–113. [Online]. Available: https://doi.org/10.1007/978-3-319-68646-2_4
 - [35] N. Pedemonte, T. Rasheed, D. Marquez-Gamez, P. Long, É. Hocquard, F. Babin, C. Fouché, G. Caverot, A. Girin, and S. Caro, *FASTKIT: A Mobile Cable-Driven Parallel Robot for Logistics*. Cham: Springer International Publishing, 2020, pp. 141–163. [Online]. Available: https://doi.org/10.1007/978-3-030-22327-4_8
 - [36] C. B. Pham, G. Yang, and S. H. Yeo, "Dynamic analysis of cable-driven parallel mechanisms," in *Proceedings, 2005 IEEE/ASME International Conference on Advanced Intelligent Mechatronics.*, 2005, pp. 612–617. [Online]. Available: <https://doi.org/10.1109/AIM.2005.1511050>
 - [37] J.-B. Izard, M. Gouttefarde, M. Michelin, O. Tempier, and C. Baradat, *A Reconfigurable Robot for Cable-Driven Parallel Robotic Research and Industrial Scenario Proofing*. Berlin, Heidelberg: Springer Berlin Heidelberg, 2013, pp. 135–148. [Online]. Available: https://doi.org/10.1007/978-3-642-31988-4_9
 - [38] A. Gonzalez-Rodriguez, F. J. Castillo-Garcia, E. Ottaviano, P. Rea, and A. G. Gonzalez-Rodriguez, "On the effects of the design of cable-Driven robots on kinematics and dynamics models accuracy," *Mechatronics*, vol. 43, pp. 18–27, 2017. [Online]. Available: <http://doi.org/10.1016/j.mechatronics.2017.02.002>
 - [39] R. Mersi, S. Vali, M. S. haghghi, G. Abbasnejad, and M. T. Masouleh, "Design and control of a suspended cable-driven parallel robot with four cables," in *2018 6th RSI International Conference on Robotics and Mechatronics (IcRoM)*, 2018, pp. 470–475. [Online]. Available: <https://doi.org/10.1109/ICRoM.2018.8657534>
 - [40] M. Rognant and E. Courteille, "Improvement of Cable Tension Observability Through a New Cable Driving Unit Design," 2018, pp. 280–291. [Online]. Available: https://doi.org/10.1007/978-3-319-61431-1_24
 - [41] Y. Zou, N. Wang, X. Wang, H. Ma, and K. Liu, "Design and Experimental Research of Movable Cable-Driven Lower Limb Rehabilitation Robot," *IEEE Access*, vol. 7, pp. 2315–2326, 2019. [Online]. Available: <https://doi.org/10.1109/ACCESS.2018.2887233>
 - [42] E. Brau and F. Gosselin, "Icare 3d: a new light 3d haptic interface," in *Proceedings of Eurohaptics*, 2006.
 - [43] F. Gosselin, "Interface haptique munie d'une structure à câbles tendus, a grand angle de manoeuvre," Patent WO2 008 080 917A1, 2006.
 - [44] W. Yi, Y. Zheng, W. Wang, X. Tang, X. Liu, and F. Meng, "Optimal design and force control of a nine-cable-driven parallel mechanism for lunar takeoff simulation," *Chinese Journal of Mechanical Engineering*, vol. 32, no. 73, 2019. [Online]. Available: <https://doi.org/10.1186/s10033-019-0382-2>
 - [45] C. Thompson and P. Campbell, "Tendon Suspended Platform Robot," Patent WO1 995 023 053A1, 1996.
 - [46] V. Collado Jimenez, L. Gustavsson, and D. Culla Irastorza, "Positioning Device Controlled by Cables," Patent WO2 011 148 004A1, 2014.
 - [47] Skycam, "Application spotlight: Yaskawa makes skycam a football hero," <https://www.youtube.com/watch?v=WSJBAn2MVDm>, accessed: 2020-11-11.
 - [48] P. H. Borgstrom, M. J. Stealey, M. A. Batalin, and W. J. Kaiser, "NIMS3D: A novel rapidly deployable robot for 3-dimensional applications," *IEEE International Conference on Intelligent Robots and Systems*, pp. 3628–3635, 2006. [Online]. Available: <https://doi.org/10.1109/IROS.2006.281718>
 - [49] J.-P. Merlet and D. Daney, "A New Design for Wire-Driven Parallel Robot," in *Inter. Cong. Design and Modelling of Mechanical Systems (CMSM 2007)*, 2007. [Online]. Available: <https://hal.inria.fr/hal-00989900>
 - [50] B. Zi, N. Wang, S. Qian, and K. Bao, "Design, stiffness analysis and experimental study of a cable-driven parallel 3D printer," *Mechanism and Machine Theory*, vol. 132, no. 2, pp. 207–222, 2019. [Online]. Available: <https://doi.org/10.1016/j.mechmachtheory.2018.11.003>
 - [51] K. Maeda, S. Tadokoro, T. Takamori, M. Hiller, and R. Verhoeven, "On design of a redundant wire-driven parallel robot warp manipulator," in *Proceedings 1999 IEEE International Conference on Robotics and Automation (Cat. No.99CH36288C)*, vol. 2, 1999, pp. 895–900. [Online]. Available: <https://doi.org/10.1109/ROBOT.1999.772403>
 - [52] A. Khajepour, S. Behzadipour, R. Dekker, and E. Chan, "Light weight parallel manipulators using active/passive cables," Patent US7 367 771B2, 2003.
 - [53] B. Zi, J. Cao, H. Zhu, and H. Sun, "Comparative study of cable parallel manipulators with and without hybrid-driven planar five-bar mechanism," *Applied Mathematical Modelling*, vol. 38, no. 24, pp. 5994–6017, 2014. [Online]. Available: <https://doi.org/10.1016/j.apm.2014.05.002>
 - [54] T. N. Le, H. Dobashi, and K. Nagai, "Configuration of redundant drive wire mechanism using double actuator modules," *ROBOMECH Journal*, vol. 3, no. 1, pp. 1–16, 2016. [Online]. Available: <https://doi.org/10.1186/s40648-016-0063-1>
 - [55] Z. Zhang, Z. Shao, L. Wang, and A. J. Shih, "Optimal design of a high-speed pick-and-place cable-driven parallel robot," in *Cable-Driven Parallel Robots*, ser. Mechanisms and Machine Science, C. Gosselin, P. Cardou, T. Bruckmann, and A. Pott, Eds., vol. 53. Cham: Springer, 2018, pp. 340–352. [Online]. Available: https://doi.org/10.1007/978-3-319-61431-1_29
 - [56] R. Chellal, E. Laroche, L. Cuvillon, and J. Gangloff, "An identification methodology for 6-dof cable-driven parallel robots parameters application to the inca 6d robot," in *Cable-Driven Parallel Robots*, ser. Mechanisms and Machine Science, T. Bruckmann and A. Pott, Eds., vol. 12. Berlin, Heidelberg: Springer Berlin Heidelberg, 2013, pp. 301–317. [Online]. Available: https://doi.org/10.1007/978-3-642-31988-4_19
 - [57] J. Zitzewitz, G. Rauter, H. Vallery, A. Morger, and R. Riemer, "Forward kinematics of redundantly actuated, tendon-based robots," in *2010 IEEE/RSJ International Conference on Intelligent Robots and Systems*, 2010, pp. 2289–2294. [Online]. Available: <https://doi.org/10.1109/IROS.2010.5649255>
 - [58] A. Pott, "Influence of Pulley Kinematics on Cable-Driven Parallel Robots," in *Latest Advances in Robot Kinematics*, J. Lenarcic and M. Husty, Eds. Dordrecht: Springer Netherlands, 2012, pp. 197–204. [Online]. Available: https://doi.org/10.1007/978-94-007-4620-6_25
 - [59] R. Pannequin, M. Jouaiti, M. Boutayeb, P. Lucas, and D. Martinez, "Automatic tracking of free-flying insects using a cable-driven robot," *Science Robotics*, vol. 5, no. 43, 2020. [Online]. Available: <https://doi.org/10.1126/scirobotics.abb2890>
 - [60] W. Yang Ho, W. Kraus, A. Mangold, and A. Pott, "Haptic Interaction with a Cable-Driven Parallel Robot Using Admittance Control," in *Cable-Driven Parallel Robots*, ser. Mechanisms and Machine Science, A. Pott and T. Bruckmann, Eds. Cham: Springer International Publishing, 2015, pp. 201–212. [Online]. Available: https://doi.org/10.1007/978-3-319-09489-2_14
 - [61] P. Miermeister, M. Lachele, R. Boss, C. Masone, C. Schenk, J. Tesch, M. Kerger, H. Teufel, A. Pott, and H. H. Bulthoff, "The CableRobot simulator large scale motion platform based on cable robot technology," in *2016 IEEE/RSJ International Conference on Intelligent Robots and*

- Systems (IROS)*. IEEE, oct 2016, pp. 3024–3029. [Online]. Available: <https://doi.org/10.1109/IROS.2016.7759468>
- [62] J.-B. Izard, A. Dubor, P.-E. Hervé, E. Cabay, D. Culla, M. Rodriguez, and M. Barrado, “Large-scale 3D printing with cable-driven parallel robots,” *Construction Robotics*, pp. 69–76, 2017. [Online]. Available: <https://doi.org/10.1007/s41693-017-0008-0>
- [63] A. Pott and V. Schmidt, “Befestigungsvorrichtung für ein seilende,” Patent DE102012024451, 2012.
- [64] X. Tang and Z. Shao, “Trajectory generation and tracking control of a multi-level hybrid support manipulator in fast,” *Mechatronics*, vol. 23, no. 8, pp. 1113 – 1122, 2013. [Online]. Available: <https://doi.org/10.1016/j.mechatronics.2013.09.002>
- [65] R. Babaghasabha, M. A. Khosravi, and H. D. Taghirad, “Adaptive robust control of fully-constrained cable driven parallel robots,” *Mechatronics*, vol. 25, pp. 27–36, 2015. [Online]. Available: <https://doi.org/10.1016/j.mechatronics.2014.11.005>
- [66] S. Qian, B. Zi, D. Wang, and Y. Li, “Development of modular cable-driven parallel robotic systems,” *IEEE Access*, vol. 7, pp. 5541–5553, 2018. [Online]. Available: <https://doi.org/10.1109/ACCESS.2018.2889245>
- [67] J. Albus, R. Bostelman, and A. Jacoff, “Modular Suspended Manipulator,” Patent US6 566 834B1, 2003.
- [68] E. Ottaviano, “A system for tension monitoring in cable-based parallel architectures,” in *12th IFToMM World Congress*, 2007.
- [69] J. C. Santos, A. Chemori, and M. Gouttefarde, “Redundancy resolution integrated model predictive control of cdprs: Concept, implementation and experiments,” in *2020 IEEE International Conference on Robotics and Automation (ICRA)*, 2020, pp. 3889–3895. [Online]. Available: <https://doi.org/10.1109/ICRA40945.2020.9197271>
- [70] S. Baklouti, E. Courteille, P. Lemoine, and S. Caro, “Vibration reduction of cable-driven parallel robots through elasto-dynamic model-based control,” *Mechanism and Machine Theory*, vol. 139, pp. 329–345, 2019. [Online]. Available: <https://doi.org/10.1016/j.mechmachtheory.2019.05.001>
- [71] T. Bruckmann, A. Pott, and M. Hiller, “Calculating force distributions for redundantly actuated tendon-based Stewart platforms,” in *Advances in Robot Kinematics*, J. Lennarčič and B. Roth, Eds. Dordrecht: Springer Netherlands, 2006, pp. 403–412. [Online]. Available: https://doi.org/10.1007/978-1-4020-4941-5_44
- [72] A. Pott, T. Bruckmann, and L. Mikelsons, “Closed-form Force Distribution for Parallel Wire Robots,” in *Computational Kinematics*, Kecskeméthy A., Müller A., Eds, A. Kecskeméthy and A. Müller, Eds. Springer, Berlin, Heidelberg, 2009, pp. 25–34. [Online]. Available: https://doi.org/10.1007/978-3-642-01947-0_4
- [73] L. Mikelsons, T. Bruckmann, M. Hiller, and D. Schramm, “A real-time capable force calculation algorithm for redundant tendon-based parallel manipulators,” in *Proceedings - IEEE International Conference on Robotics and Automation*, 2008, pp. 3869–3874. [Online]. Available: <https://doi.org/10.1109/ROBOT.2008.4543805>
- [74] Fit, “Matlab fit,” <https://fr.mathworks.com/help/curvefit/fit.html>, accessed: 2021-01-13.